DRAFT
Microwave Radiometer Profiler Handbook

Evaluation of a New Multi-Frequency Microwave Radiometer for Measuring the Vertical Distribution of Temperature, Water Vapor, and Cloud Liquid Water

Prepared by

James C. Liljegren
Environmental Research Division
Argonne National Laboratory
December 4, 2002

For the

DOE Atmospheric Radiation Measurement (ARM) Program

Table of Contents

Figures

Abstract

The U. S. Department of Energy's Atmospheric Radiation Measurement (ARM) Program has a critical need to continuously characterize the vertical distribution of temperature, water vapor, and clouds at its Cloud and Radiation Testbed (CART) facilities. These data are needed to support a wide range of models of atmospheric processes, in particular single-column and cloud-resolving models. To address this need, Radiometrics Corporation has developed a new multi-frequency microwave radiometer profiler (MWRP) under a DOE grant, which will provide continuous measurements of the vertical distributions of temperature, water vapor, and cloud liquid water from the ground up to 10 km for all non-precipitating conditions. The MWRP has been deployed at ARM CART sites near Lamont, OK and Barrow, AK during 2000-2002 for evaluation. This report presents the results of this three-year evaluation in terms of the reliability of the hardware, the accuracy of the radiometric measurements, and the skill of the retrieval algorithms. The report concludes with recommendations for deployment and further algorithm development.

1.0 Introduction

1.1 Motivation

The U. S. Department of Energy's Atmospheric Radiation Measurement (ARM) Program has a critical need to characterize the vertical distribution of temperature, water vapor, and clouds at its Cloud and Radiation Testbed (CART) facilities. These data are needed to support a wide range of models of atmospheric processes, in particular those associated with radiation transfer and clouds. ARM currently acquires vertical profiles of temperature and water vapor primarily by launching radiosondes. At the Southern Great Plains (SGP) CART central facility radiosondes are launched every 6 hr, every day of the year. At approximately $200 per launch for materials and labor, this amounts to nearly $300,000 per year. Despite this expense, these routine launches from a single location are inadequate to provide the spatial and temporal characterization of the atmosphere needed by the ARM Cloud Parameterization and Modeling Working Group (CPMWG) for driving single-column models (SCMs) and cloud-resolving models (CRMs).   To support the CPMWG, radiosondes are launched at three-hour intervals from each of four SGP boundary facilities plus the central facility during annual or semi-annual 21-day intensive operation periods (SCM IOPs) for an additional cost of over $150,000 per IOP. However, the limited frequency and duration of these SCM IOPs, due to the expense of the soundings, adversely affect the ability of the CPMWG to advance the state of the art in cloud parameterizations, as explained by Randall et al. (2000) in the *ARM Vision 2000* report of the CPMWG. For SCM IOPs the remaining SGP CART instruments, including sophisticated cloud radars and lidars, might as well operate only during these 21-day IOPs. The ability to acquire *continuous* thermodynamic profiles of temperature, water vapor, and cloud liquid water from

each of the boundary facilities is necessary to achieve a *continuous*, 365-day per year SCM IOP and to make better use of the full array of SGP CART instrumentation.

Even if radiosondes could be launched routinely at the boundary facilities, their temporal and vertical resolution do not match well with the SCM and CRM needs. Radiosondes take about 40 min to ascend through the troposphere and about 2 hr to ascend to full height. Practical considerations further limit the launch frequency to a minimum of 3 hr. In contrast, SCMs have time steps of 10-30 min, and CRMs have time steps of about 10 sec (Ghan et al. 2000). Conversely, whereas SCMs have approximately 20 vertical layers and CRMs have 30-50 vertical layers, ranging in thickness from roughly 100 m near the ground to about 1000 m aloft, radiosondes have a much higher vertical resolution, about 10 m. Modelers generally reduce the vertical resolution of the soundings by averaging over the vertical layers of the model.

In an attempt to acquire profile measurements with temporal and spatial characteristics more appropriate for these models, ARM has deployed a variety of ground-based remote sensors. However, none of these can provide a complete profile of tropospheric temperature or water vapor for both clear and cloudy conditions both day and night. None offers the high reliability of the balloon-borne sounding system (BBSS). The non-commercially produced remote sensors that have been fielded by ARM are particularly fragile and extremely expensive to maintain or repair. Consequently, the BBSS remains the primary profiling instrument.

To address this problem, a new microwave radiometer profiler (MWRP) was developed for ARM by Radiometrics Corporation under a DOE Small Business Innovative Research (SBIR) grant. The potential offered by this new radiometer is illustrated by the time-height contours of temperature, water vapor density, and cloud liquid water content presented in Figure 1 for 1-2 April 2002 at the SGP CART site, and in Figure 2 for 19-24 December 2000 at the

North Slope of Alaska (NSA) CART site at Barrow, Alaska. In Figure 1, the surface temperature inversion is readily discernable on both nights; a warming and moistening trend is observed followed by the arrival of a cold front at 12:00 UTC (06:00 LST) on 2 April accompanied by low clouds as indicated by the temperature of the infrared thermometer (IRT; black line, top panel), the liquid water path (white line, bottom panel) and the liquid water content. In Figure 2, a general warming and moistening trend that occurred over several days is captured in addition to the persistent temperature inversion. During this period one radiosonde was launched each day on 19-22 December; none were launched on 23-24 December, which fell on a weekend.

Under the terms of the SBIR grant, one MWRP has been delivered to the ARM Program for evaluation. This report describes the results of that evaluation.
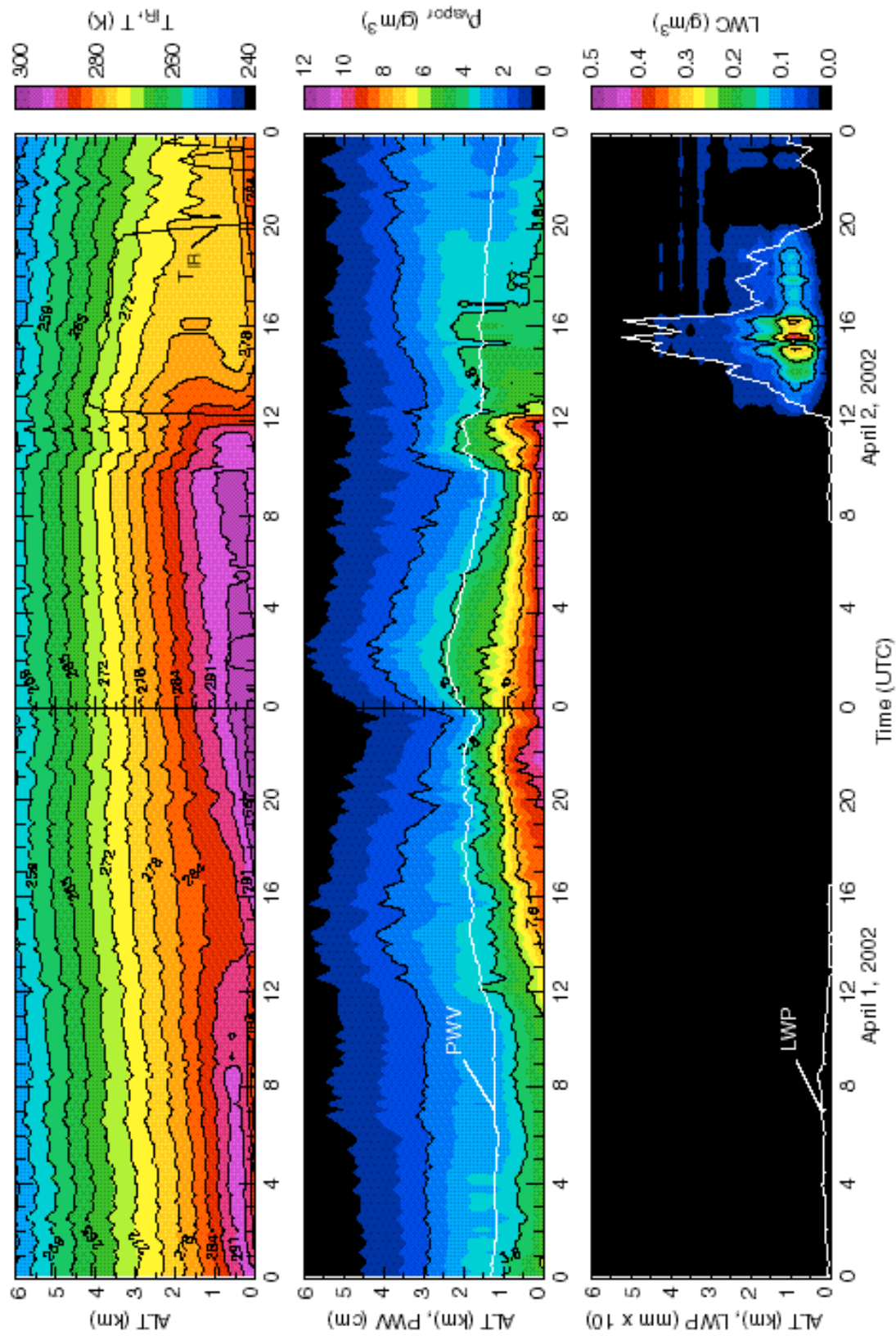
Figure 1. Time-height contours of temperature (top), water vapor density (middle), and liquid water content (bottom) for 1-2 April 2002 at the SGP CART site near Lamont, OK. The heavy black line in the top panel indicates the temperature reported by the infrared thermometer (IRT). The heavy white lines in the middle and bottom panel indicate the precipitable water vapor (PWV) and liquid water path (LWP), respectively.

11
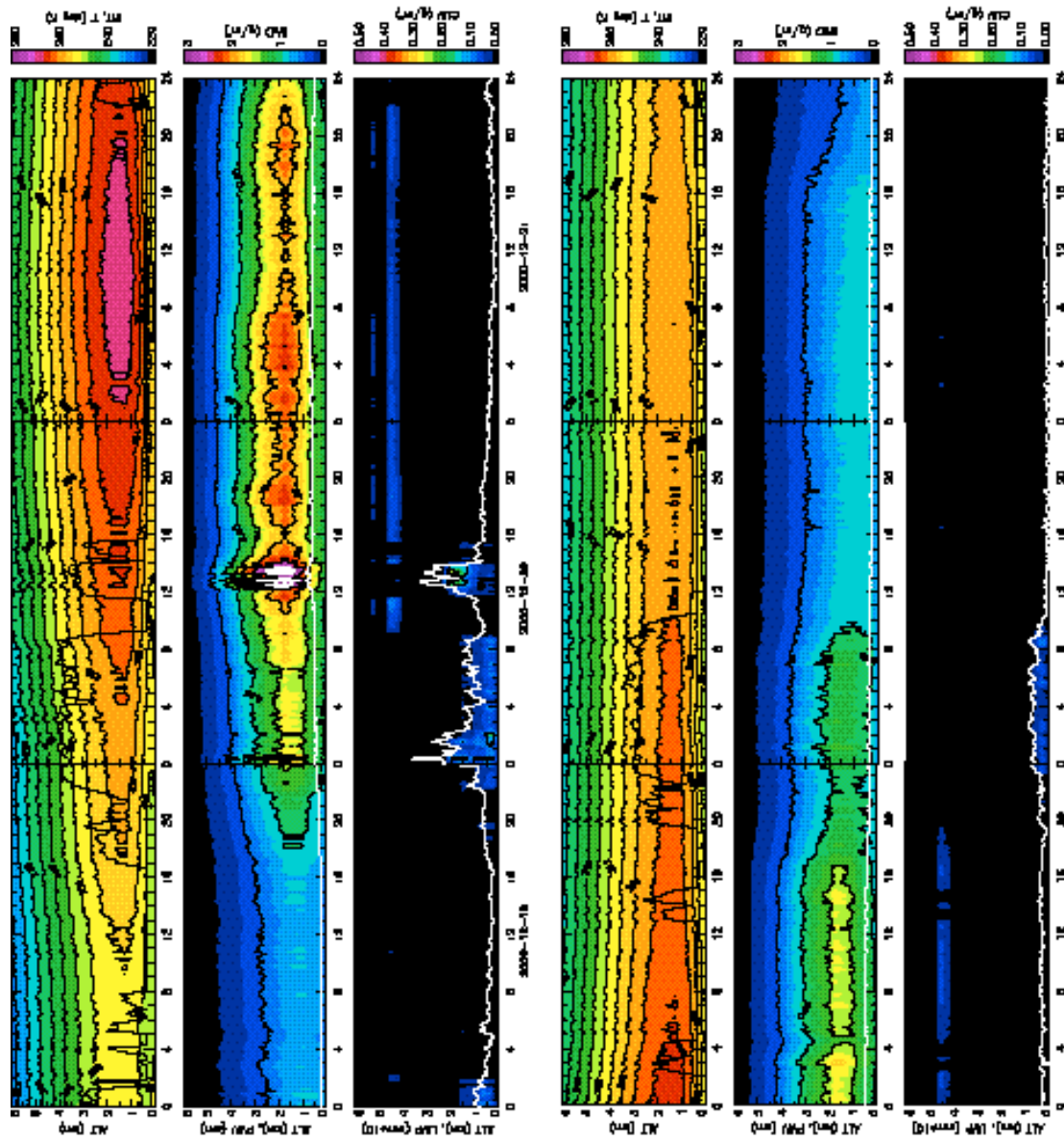
Figure 2. Time-height contours of temperature (top), water vapor density (middle), and liquid water content (bottom) for 19-24 December 2000 at the NSA CART site at Barrow, AK. The heavy black line in the top panel indicates the temperature reported by the infrared thermometer (IRT). The heavy white lines in the middle and bottom panel indicate the precipitable water vapor (PWV) and liquid water path (LWP), respectively.

12

1.2 The Microwave Radiometer Profiler

Absorption and emission of microwave radiation in the range 10-80 GHz are dominated by molecular water vapor and oxygen, as well as cloud liquid water. In Figure 3, the absorption due to the water vapor resonance at 22.235 GHz and the band of oxygen resonances near 60 GHz is shown near the surface (solid lines) and at 2 km (dashed lines) based on the mean vertical profiles of temperature and water vapor during the summer at the SGP. The absorption due to cloud liquid water at 283 K (dot-dashed line) is also presented. Because the mixing ratio of oxygen is invariant with altitude the emission at each altitude depends on the local temperature; the variation of emission with frequency permits radiation from a range of altitudes to reach the instrument, thereby permitting the vertical temperature distribution to be retrieved. The emission due to water vapor varies in proportion to the water vapor density; it also depends on altitude due to the effect of pressure broadening on the line shape, thereby permitting the vertical distribution of water vapor density to be retrieved. The variation of liquid water absorption approximately as the square of frequency permits a coarsely resolved vertical distribution of liquid water retrieval to be attempted. The MWRP measures the microwave radiance, expressed as brightness temperature, at 5 frequencies near the water vapor resonance centered at 22.235 GHz and 7 frequencies in the band of oxygen resonances between 51 and 59 GHz. These were selected based on an eigenvalue analysis by Solheim et al. (1998) and are indicated in Figure 3 by the vertical grey lines. The radiometer specifications, provided by Radiometrics, are summarized in Table 1.
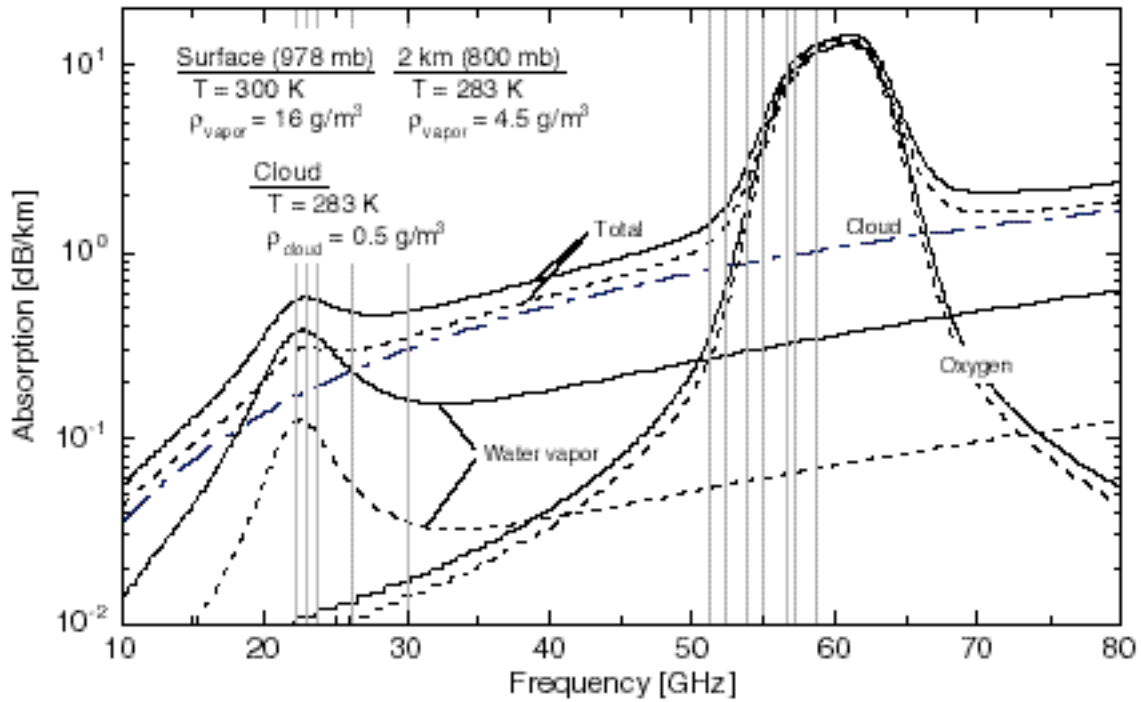
Figure 3. The microwave absorption spectrum for water vapor and oxygen calculated for mean summer conditions at the surface (solid) and at 2 km (broken). The cloud liquid water absorption (dot-dashed) is also given for a a liquid water content of 0.5 g/m^3 and 283 K.

Table 1. Microwave radiometer profiler specifications.

K-band (water vapor) sensing frequencies (GHz)	22.235, 23.035, 23.835, 26.235, 30.0
V-band (temperature) sensing frequencies (GHz)	51.25, 52.28, 53.85, 54.94, 56.66, 57.29, 58.80
Bandwidth (double side band, MHz)	200
Beam width (full width at half power)	6.1° at 22 GHz 4.7° at 30 GHz 2.4° at 51 GHz 2.2° at 59 GHz
Radiometric accuracy	0.5 K
Radiometric repeatability	0.25 K

Accuracy of meteorological sensors
    Barometric pressure
    Temperature
    Relative humidity
	
	0.3 mb
	0.5 °C
	2%

Accuracy of Heimann infrared thermometer (IRT)	0.5 °C + 0.7% of the difference between IRT housing and observed target temperatures

The instrument uses neural network retrieval algorithms to determine the vertical distribution of temperature, water vapor, and cloud liquid water at 47 levels for all non-precipitating conditions: 11 levels from the ground to 1 km at 100-m spacing, then 36 levels at 250-m spacing up to 10 km. The retrievals are derived using a standard back-propagation algorithm for training and a standard feed-forward network for profile determination, as described by Solheim, et al. (1998).

1.3 Evaluation Approach

The evaluation focused on three key aspects of performance: (1) the reliability and robustness of the hardware; (2) the accuracy of the radiometric brightness temperatures and the stability of the calibrations; and (3) the skill of the retrieval algorithms. Each of these will be described in subsequent sections, followed by conclusions and recommendations.

2.0 Hardware Reliability

The reliability of an instrument over time and its robustness over a wide range of operating conditions are a key aspect of performance. Not only does reliability control the quantity of data provided by the instrument, but it is also the principal driver of the operating cost. The latter is especially true for remote deployment locations.

To assess its reliability and robustness, the MWRP was deployed at the SGP and NSA CART sites for extended periods, as indicated in Table 2.

Table 2. MWRP deployment periods and locations.

Period	Location	Remarks
25 February-22 March 2000	Blackwell-Tonkawa airport	Cloud IOP

	Blackwell, Oklahoma	
23 March-8 August 2000	SGP Central Facility Billings, Oklahoma	Surface temperature range min: -5 °C max:46 °C
15 August-8 September 2000	Radiometrics Corp. Boulder, Colorado	Added insulation and a heater to the IR thermometer.
15 September 2000-4 April 2001	NSA Central Facility Barrow, Alaska	Surface temperature range min: -36 °C max:7 °C
11 April-24 June 2001	Radiometrics Corporation Boulder, Colorado	Synthesizer replaced.
29 June 2001-31 October 2002	SGP Central Facility Billings, Oklahoma	Surface temperature range min: -14 °C max:44 °C
4 November-3 December 2002	Radiometrics Corporation Boulder, Colorado	Synthesizer replaced.

Table 2 also lists the range of surface temperatures experienced by the MWRP at each location. During the NSA deployment the surface temperature fell as low as –36 °C with an average temperature of –18 °C; at the SGP the surface temperature rose as high as 46 °C. Despite these temperature extremes, thermal stabilization of the radiometer was maintained at all times. This was achieved by setting the stabilization temperature to 20°C at the NSA and to 50!°C at the SGP.

The most serious operational problem at the NSA was the accumulation of freezing rain on the sides of the polycarbonate foam window; the heater/blower was only able to keep the top of the window clear. After the NSA deployment, Radiometrics determined that the frequency synthesizer was exhibiting degraded performance and replaced at their expense. At the SGP the disk drive in the laptop computer crashed during installation in June 2001. In mid-July 2002, after about a year of continuous operation, the frequency synthesizer began to exhibit degraded performance; it was replaced in November 2002 at a cost to ARM of $8,000. The synthesizer

installed in late 2002 is a "third generation" unit (whereas the earlier units had been "first generation") and is expected to be more robust.

The availability and quality of the data during these deployments is depicted graphically in Figure 4. The data was considered available (black) if a data record existed; data was considered good (green) if it passed a series of min/max checks and the moisture sensor was off; data was considered bad (red) if it failed the min/max checks. Most of the gaps in the data shown in Figure 4 are due to power outages, although a few computer problems also arose. The data availability statistics for the SGP and NSA deployments are presented in Table 3. The lower data quality percentage for NSA reflects problems with freezing rain and hoar frost forming on the instrument. Since the time of the NSA deployment Radiometrics has developed a blower/heater with a greater airflow, greater heat output, and greater window coverage to address this problem. The differences between the "bad" data quality percentage and the "wet" percentage reflect the problem of false positive (sensor ON when no moisture is present) and false negative (sensor OFF when moisture is present) indication. This problem arises due to the temperature dependent nature of the sensor, which requires seasonal adjustment.
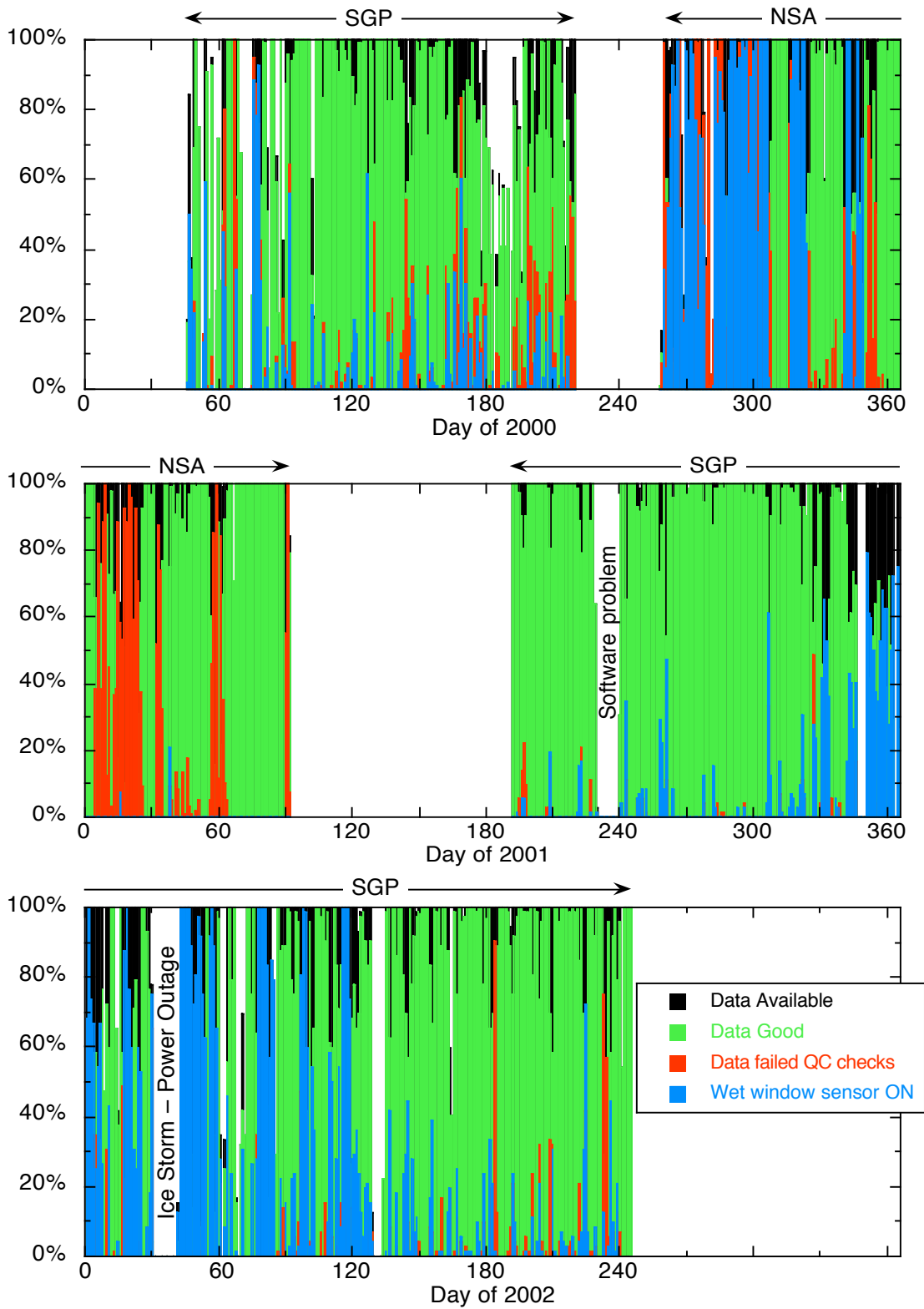
Figure 4. Data availability and quality. Most gaps are due to power outages.

18

Table 3. Overall data availability and quality statistics.

	Available (%)	Good (%)	Bad (%)	Wet (%)
SGP	88	72	7	14
NSA	97	57	34	23

3.0 Measurement Accuracy

The frequency-dependent microwave radiance, reported as a brightness temperature T_B is the fundamental quantity measured by the radiometer. The accuracy of the brightness temperature measurements is critical to obtaining accurate retrievals of atmospheric state parameters. The measurement accuracy depends on the quality and stability of the hardware as well as on the accuracy and precision of the calibration, which can be difficult to separate. In this section the measurement accuracy is evaluated by analysis of the calibration data and through direct and indirect comparisons with other instruments. A detailed investigation of the calibration procedures and algorithms is beyond the scope of this study.

At each frequency the signal voltage V_{sky} resulting from a sky measurement is transformed to a brightness temperature according to the expression

$$T_B = T_{ref} - G^{-1}\left(V_{ref} - V_{sky}\right) \tag{1}$$

where T_{ref} is the (near ambient) temperature of an internal blackbody reference target, V_{ref} is the signal voltage resulting from a measurement of the reference target, and G is the radiometer gain given by

$$G = \left(V_{hi} - V_{lo}\right)/\left(T_{hi} - T_{lo}\right) \tag{2}$$

where T_{hi} and V_{hi} are the temperature and signal voltage associated with a high temperature reference and T_{lo} and V_{lo} are associated with a low temperature reference. In the case of the

MWRP, the low temperature reference is provided by the internal blackbody target such that $T_{lo}=T_{ref}$. The high temperature reference is achieved by adding a noise injection temperature T_{nd} from a calibrated noise diode such that $T_{hi} = T_{ref} + T_{nd}$. The gain is then calculated as

$$G = \left(V_{ref+nd} - V_{ref}\right)/T_{nd} \tag{3}$$

where $V_{ref+nd} - V_{ref}$ is the difference in signal voltages recorded when viewing the internal target with and without the noise diode switched on. The value of T_{nd} is calibrated as follows. First the gain is determined using

$$G = \left(V_{ref} - V_{cold}\right)/\left(T_{ref} - T_{cold}\right) \tag{4}$$

where T_{cold} and V_{cold} correspond to the temperature and signal voltage of a cold external reference. Then (3) and (4) are combined to yield

$$T_{nd} = \left(T_{ref} - T_{cold}\right)\left(\frac{V_{ref+nd} - V_{ref}}{V_{ref} - V_{cold}}\right). \tag{5}$$

Because the K-band (22-30 GHz) and V-band (51-59 GHz) receivers operate over different ranges of brightness temperature, different methods of providing the cold external reference temperature are utilized.

3.1 K-band channels (22-30 GHz)

The water vapor resonance centered at 22.235 GHz is weakly absorbing so the optical thickness increases linearly with increasing water vapor amount. Consequently, the tipping curve method is used to provide the cold reference temperatures in the 10-90 K range necessary to calibrate the K-band channels. The tipping curve method exploits the linear relationship between optical thickness and atmospheric path length that holds when the sky is free of liquid

water clouds and strong horizontal water vapor gradients to derive the zenith brightness temperature, which serves as T_{cold} in (5), from which T_{nd} is determined.

The MWRP acquires tipping curve measurements continuously, at about 15-minute intervals. These are screened for valid sky conditions based on the linearity of the regression of optical thickness on path length ("air mass") by requiring that the correlation coefficient exceed 0.99. Since the MWRP was redeployed to the SGP in June 2001, over 26,000 valid tipping curves have been acquired. A statistical summary of the values of T_{nd} derived from these tipping curves is graphically depicted in Figure 5. The filled circles indicate the monthly means for 2001 (black) and 2002 (grey); the error bars indicate twice the standard deviation, which represents about 96% of the range of values.
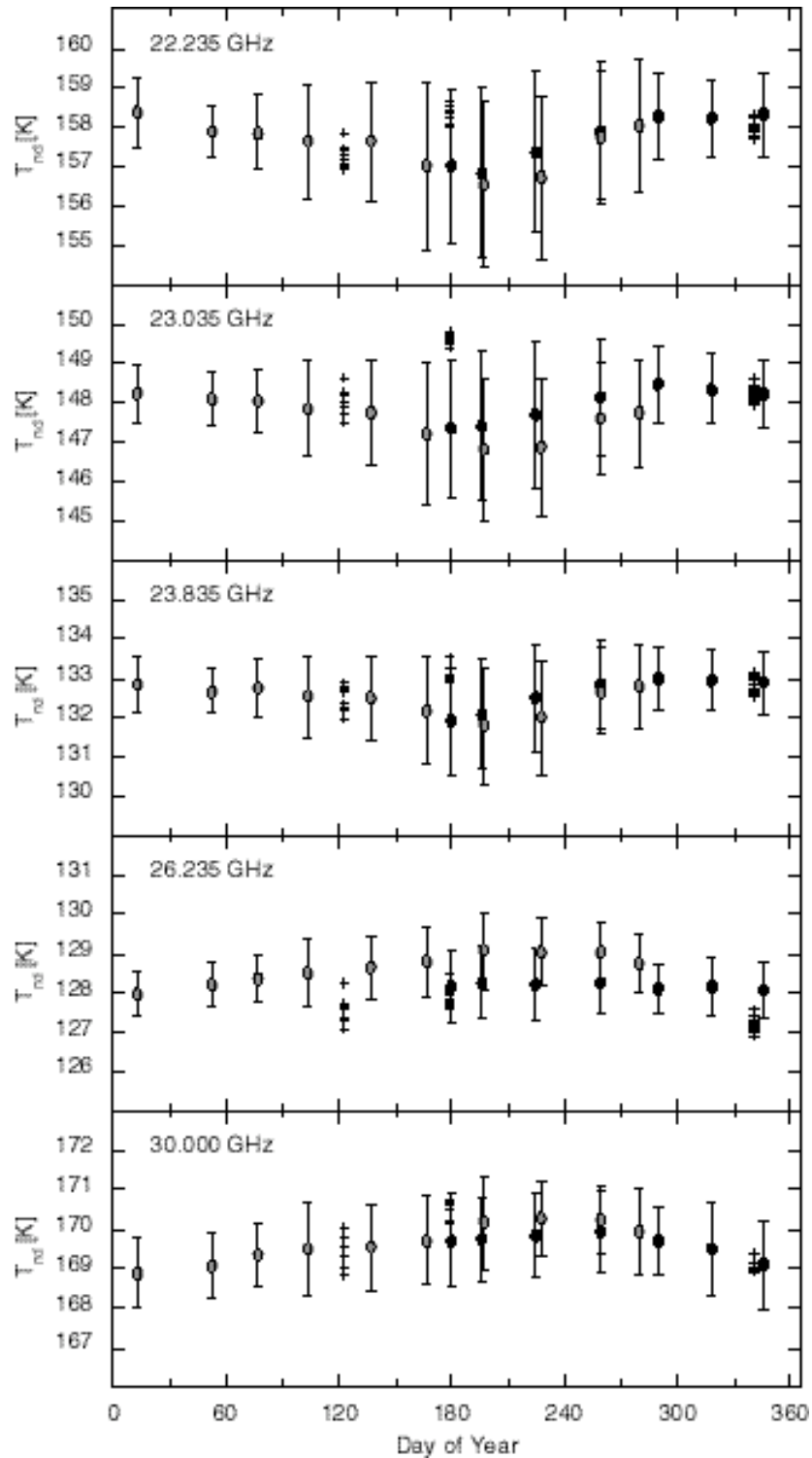
Figure 5. Monthly mean noise injection temperatures T_{nd} derived from tipping curves for 2001 (black circles) and 2002 (grey circles). The error bars indicate twice the standard deviation or 96% of the range of values. Individual values of T_{nd} derived from liquid nitrogen calibrations are indicated by crosses.

The statistics depicted in Figure 5 address the issue of the long-term stability of the K-band receiver and the calibration. The inter-annual variation in the monthly means is generally very small (<1%) and in no case exceeds the spread for the month. It is also apparent that the values of T_{nd} vary seasonally, which reflects a weak dependence on temperature. To account for this, temperature correction coefficients have been determined for each channel based on a linear fit of T_{nd} to T_{ref}. The corrections are used to adjust the individual values of T_{nd} to a nominal reference temperature (290 K). The adjusted values are low-pass filtered: $y_i = ax_i + (1-a)y_{i-1}$ where a = 0.1. The most recent low-pass filtered values of T_{nd} are then adjusted to the current value of T_{ref} prior to being used in (3) to calculate the gain.

The small crosses on days 122, 179, and 340 in Figure 5 indicate values of T_{nd} determined using a liquid nitrogen-filled external target to provide the cold temperature reference in (5). For the most part these values are consistent with the results of the tipping curve calibrations. However, the results for the 23.035 GHz channel on day 179 in 2001 are more than two standard deviations away from the mean of the tipping curve-derived values for that channel; the results for the 22.235 and 23.835 GHz channels on this day are more than one standard deviation from the mean. This upward bias could have resulted from condensation forming on the bottom of the liquid nitrogen target, which would have caused the effective target temperature to be greater than that used to compute T_{nd}; however, no such errors were observed in the calibration data for the V-band (temperature sensing) channels. Also, the spread of the liquid nitrogen-derived results is relatively large, comparable to the monthly standard deviation of the tipping curve-derived results in most cases. Although this suggests that the liquid nitrogen-filled target is inferior to the tipping curve procedure for providing a cold temperature calibration reference for

the K-band channels, the number of liquid nitrogen-derived values is insufficient to draw a firm

conclusion in this regard.

To assess the accuracy of the brightness temperatures measured by the MWRP, the

measurements at 23.835 and 30.0 GHz were compared with brightness temperatures measured

by a two-channel microwave radiometer (MWR) at 23.8 and 31.4 GHz. The calibration of the

MWR is described by Liljegren (2000). The differences between the MWRP and MWR

brightness temperatures are presented as functions of the MWR brightness temperature in

Figures 6 and 7. Because these comparisons are not at exactly the same frequencies, the

predicted differences based on the Rosenkranz (1998) absorption models for oxygen and water

vapor are also indicated. The statistics are summarized in Table 4.

Table 4. Brightness temperature difference ΔT_B statistics for the comparison of MWRP and MWR during 2000-2002 under liquid-water-free sky conditions.

	2000	2001	2002	Model[†]
Number of samples	8650	7202	13,711	
23.835 – 23.8 GHz				
Slope of ΔT_B vs T_B regression, K/K	0.005	0.036	0.030	-0.009
Regression root-mean-square error, K	1.03	0.70	0.67	
Mean ΔT_B (bias), K	0.14	0.59	0.48	
Standard deviation ΔT_B, K	1.03	0.93	0.82	
30.0 – 31.4 GHz				
Slope of ΔT_B vs T_B regression, K/K	-0.016	0.089	0.070	0.048
Regression root-mean-square error, K	0.79	0.51	0.51	
Mean ΔT_B (bias), K	0.08	0.43	0.32	
Standard deviation ΔT_B, K	0.79	0.73	0.66	

[†]Rosenkranz, 1998.
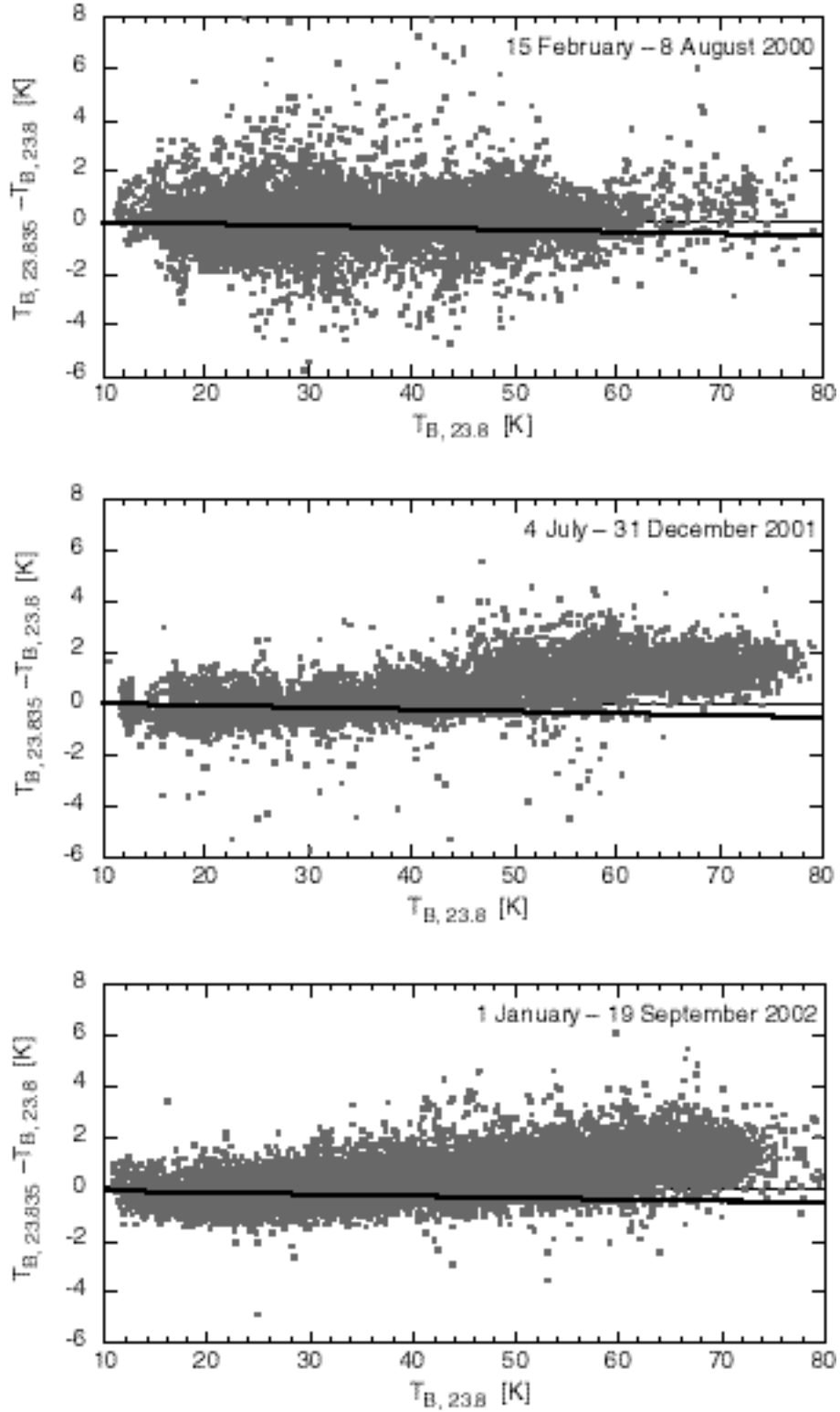
Figure 6. Differences in measured brightness temperature between the MWRP at 23.835 GHz and the collocated two-channel MWR at 23.8 GHz at the SGP. The heavy black line indicates the differences between model-calculated brightness temperatures at these frequencies.
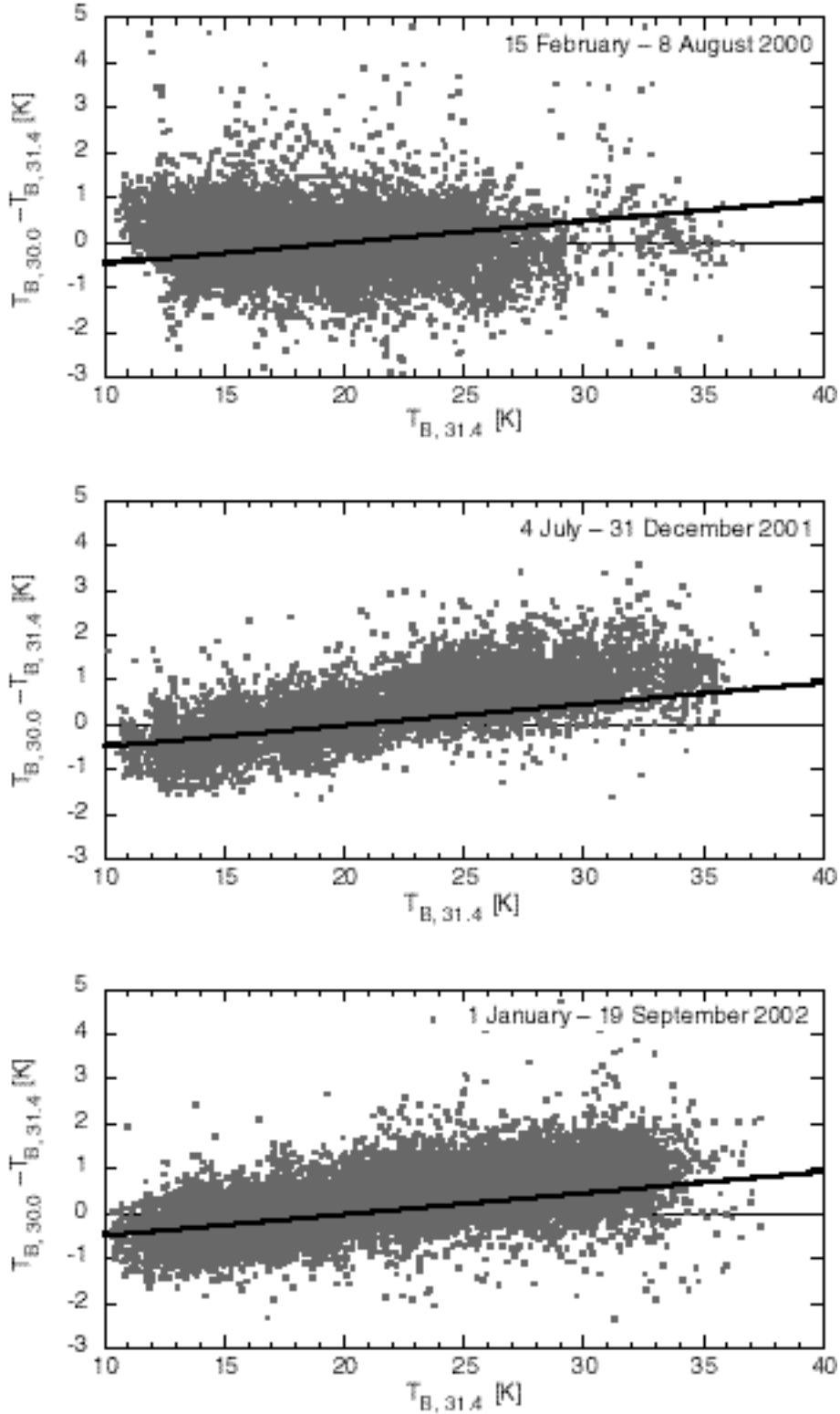
Figure 7. Differences in measured brightness temperature between the MWRP at 30.0 GHz and the collocated two-channel MWR at 31.4 GHz at the SGP. The heavy black line indicates the differences between model-calculated brightness temperatures at these frequencies.

26

The results do not appear to be entirely consistent over all three years: for both the 23.8 and 31.4 GHz comparisons, the mean difference is near zero over the range of brightness temperatures in 2000 whereas for 2001 and 2002 the mean difference is near zero for the lower end of the brightness temperature range but shows increasing bias (MWRP higher) with increasing brightness temperature. The latter behavior appears to agree with the model-predicted trend at 31.4 GHz; however, the correlation with the trend at 23.8 GHz suggests this may also be a coincidence. The difference in behavior between 2000 and 2001-2002 may be due to modifications made to the radiometer by Radiometrics after it was returned from Barrow, Alaska in the spring of 2001. The explanation of the observed trends in the measured brightness temperature differences between the MWRP and MWR is not clear and will require a detailed analysis of the tipping curve reduction algorithms implemented in the MWRP to determine. Despite this, the mean brightness temperature difference is generally less than the claimed 0.5 K accuracy of the MWRP and the regression root-mean-square (due to variations in both the MWR and MWRP) is only slightly larger than $\sqrt{2}$ times the claimed repeatability of 0.25 K.

To assess the accuracy of all five K-band channels, comparisons were carried out with model-calculated brightness temperatures. Of course, such a comparison depends on the accuracy of the model as well as the accuracy of the profiles of pressure, temperature, and water vapor used to drive the model. The Rosenkranz (1998) absorption models were used in the brightness temperature calculations. To overcome the known dry bias of the radiosonde relative humidity sensors as well as to reduce the variability in their calibration, the ARM linearly scaled sounding product (sgplssondeC1.c1) was used to drive the model. In this product the measured radiosonde relative humidity is linearly scaled by the ratio of the integrated water vapor amount from a collocated two-channel MWR to that of the original sounding. Ratios of measured-to-

modeled brightness temperatures are presented in Figure 8 for the 2001-2002 deployment at the

SGP. The blue circles indicate the case where the collision-broadened width parameter γ_C of the

22.235 GHZ water vapor line used in the model calculations was the original value supplied by

Rosenkranz; the red circles indicate the case where the width was reduced to 95% of the original

value (per conversation with S. A. Clough). Statistics corresponding to the results in Figure 8

are presented in Table 5.
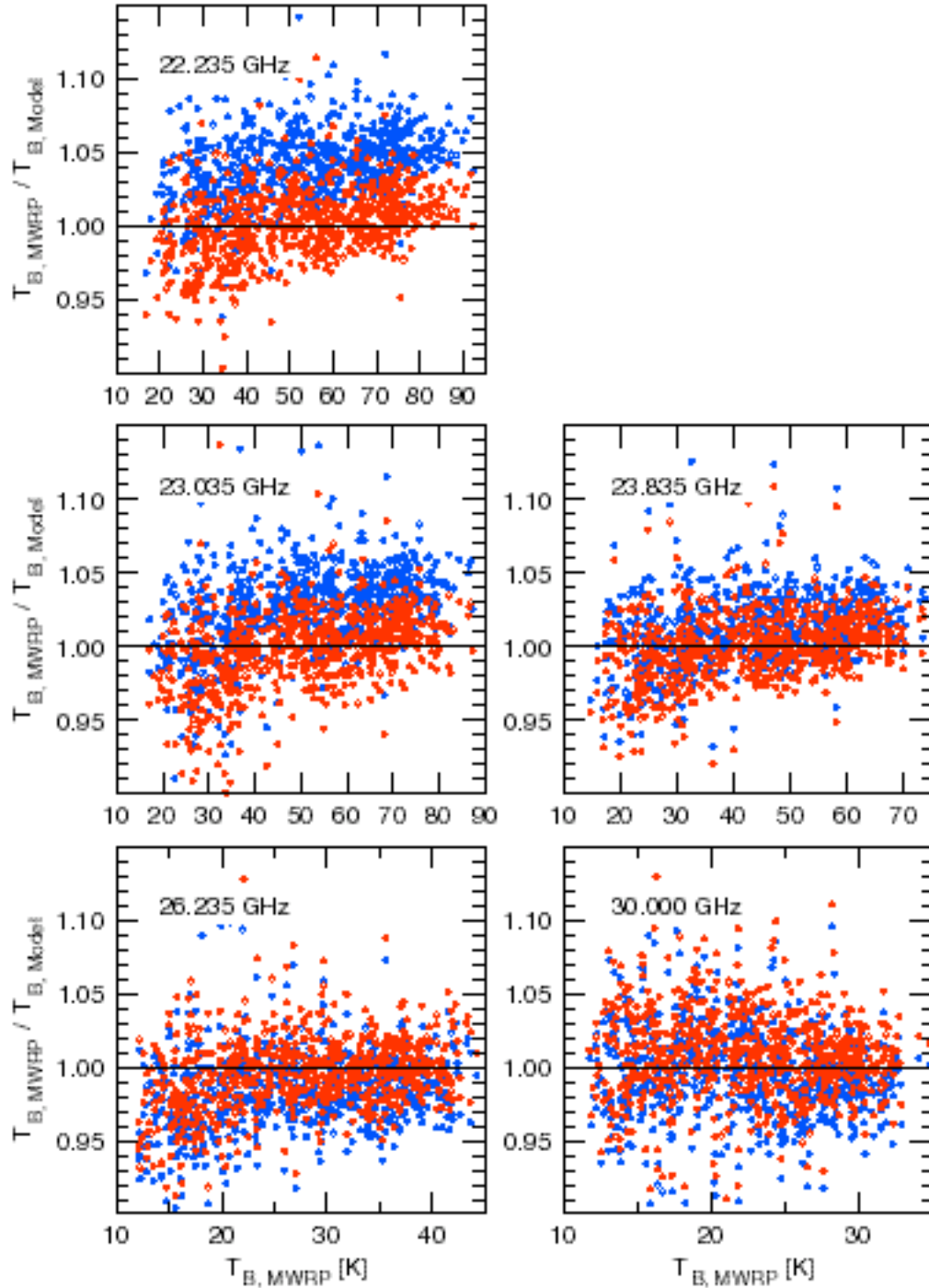
Figure 8. Ratios of measured and modeled brightness temperatures at the K-band frequencies for both the original value of the width parameter (blue) provided with the Rosenkranz (1998) water vapor absorption model and 95% of the original value (red).

29

Table 5. Statistics of the ratio $T_{B, MWRP}/T_{B, Model}$ at the five K-band frequencies using the original and reduced collision-broadened line width parameter γ_C for 719 clear-sky comparisons at the SGP during 2001-2002.

	Mean		Std. Dev.	
Frequency, GHz	1.0 γ_C	0.95 γ_C	1.0 γ_C	0.95 γ_C
22.235	1.040	1.003	0.026	0.025
23.035	1.026	0.998	0.029	0.028
23.835	1.013	1.001	0.026	0.025
26.235	0.984	0.996	0.026	0.026
30.000	0.997	1.009	0.032	0.032

Although the trend of increasing ratio with increasing brightness temperature reflects the earlier trend of the MWRP–MWR comparison, nevertheless the results clearly show that reducing the line width substantially improves the agreement between the measurements and the model. Not only is this an important result in its own right, but it also demonstrates the consistency of the measured brightness temperatures across the five K-band channels.

The scatter in these comparisons reflected in the standard deviation of the ratios is not affected by the reduction in line width. This scatter results from variations in the sounding data and the MWR data used to scale the soundings as well as the MWRP measurements. This suggests that the accuracy of the MWRP K-band channels is better than 2.5-3.0%, consistent with the MWRP–MWR comparisons summarized in Table 4.

3.2 V-band channels (51-59 GHz)

The strongly absorbing oxygen resonances in the 51-59 GHz range cause the relationship between optical thickness and absorber amount or atmospheric path length to be non-linear, which precludes the use of the tipping curve method for calibration. Instead, because the lowest brightness temperature measured at the least absorbing frequency (51.25 GHz) is about 100 K, a

liquid nitrogen-filled external target is used to provide the ~77 K cold temperature reference needed to determine T_{nd} in (5). As shown in Figure 9, the external target is comprised of a very low absorption thick-walled Styrofoam™ container with a blackbody target placed inside on the bottom and filled with 25-30 liters of LN_2. Alternating measurements of the near ambient internal and cold external targets are performed for up to an hour, or until condensation forms on the bottom of the Styrofoam container. The heated blower normally used to prevent dew from condensing on the polycarbonate foam window of the radiometer is manually cycled on and off to delay the formation of condensation on the bottom of the container.

Figure 9. The Microwave Radiometer Profiler (MWRP) at Barrow, Alaska with the LN_2-filled Styrofoam target in place during calibration of the V-band channels in September 2000.

The brightness temperature measured by the MWRP when viewing the LN$_2$ target is elevated ~2K above the boiling point of LN$_2$, which depends on atmospheric pressure, due to a number of effects, principally reflection at the interface between the Styrofoam and LN$_2$ (~1.7 K), the absorption of the Styrofoam (~0.2K), and the elevation of the boiling point of LN$_2$ due to the hydrostatic pressure of the 20 cm column of LN$_2$ above the bottom of the container (~0.2K) as discussed by Solheim (1993). Corrections for these effects are included in the calibration process. No attempt has been made in this evaluation to verify these corrections.

Since the V-band receiver was upgraded in the spring of 2001, four LN$_2$ calibrations have been performed. The results of these calibrations are summarized in Table 5. The standard deviations of the LN2-derived values of T_{nd} over the 11-month period shown have generally been less than 1% of the mean, except for the 52.85 GHz channel, which was slightly above 1%. This demonstrates good calibration stability.

Table 6. Statistics of temperature-corrected T_{nd} at the seven V-band measurement frequencies for the LN$_2$ calibrations performed at the Radiometrics facility in Boulder, CO and at the SGP during 2001-2002.

Location	Date	51.25 GHz	52.28 GHz	53.85 GHz	54.94 GHz	56.66 GHz	57.29 GHz	58.80 GHz
Boulder	Jun 2001	242.65	231.05	210.10	194.26	196.76	202.81	217.23
SGP	Jun 2001	243.68	229.87	209.42	194.67	196.79	203.44	216.76
SGP	Dec 2001	244.29	235.66	212.91	196.58	196.87	204.18	217.60
SGP	May 2002	243.83	234.87	210.52	194.71	197.61	205.24	218.47
Mean		243.61	232.86	210.74	195.05	197.01	203.92	217.51
Standard Deviation		0.69	2.83	1.52	1.04	0.41	1.04	0.73
Std Dev/Mean (%)		0.29	1.22	0.72	0.53	0.21	0.51	0.33

Because a direct comparison of measured brightness temperatures with another instrument was not possible, a comparison with model-calculated brightness temperatures was

performed. Again the Rosenkranz (1998) absorption models were used with input profiles of pressure, temperature, and water vapor supplied by radiosondes. MWRP–Model brightness temperature differences are presented in Figure 10 as a function of the day of the year. The colors indicate the calibration in effect at the time of the measurement, including the deployment at Barrow, Alaska. Summary statistics are provided in Table 7.
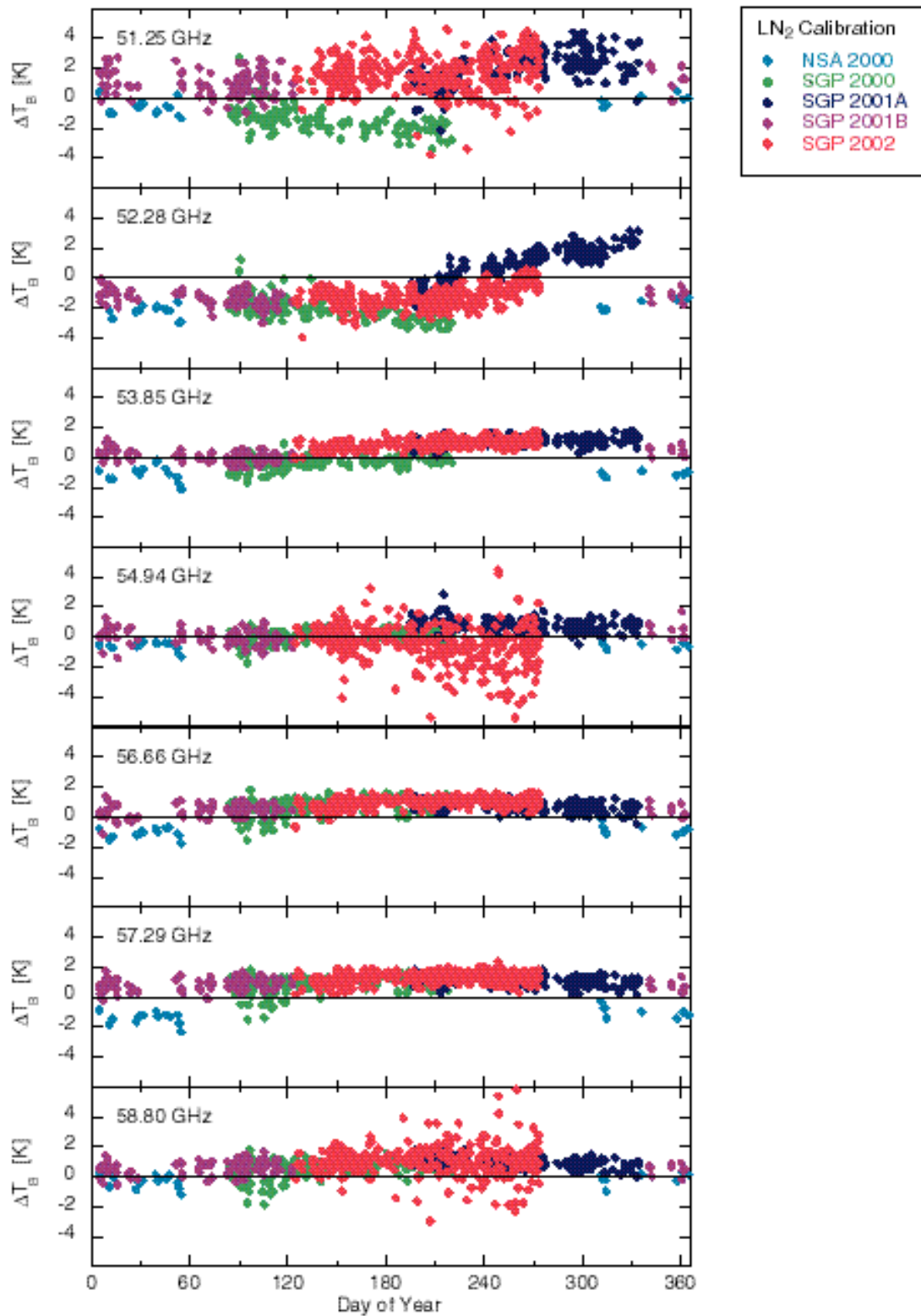
Figure 10. Brightness temperature differences (measured – modeled) for the V-band channels under clear-sky conditions during 2000-2002. The colors indicate the calibration in effect at the time.

Several features are evident in the comparison results. First, the measured T_B values generally agree 1-2 K with the model-calculated values. These biases could be due to shortcomings in the model or may reflect the limit of the liquid nitrogen calibration procedure. Also, the results are generally very consistent over time. The exceptions are at 51.25 GHz for the SGP 2000 calibration and at 52.28 GHz for the SGP 2001A calibration, where substantial drift in the calibration is evident. In both of these instances, it appears that the drift did not continue after the instrument was recalibrated. Radiometrics recommends monthly calibrations; however, this may not be practical at remote locations. The data indicate that semi-annual calibrations are sufficient, but regular calibration checks by comparison against model-calculated values would be helpful to detect drifts that may require a recalibration to be performed.

Table 7. Brightness temperature difference ΔT_B statistics (MWRP–Model) at the seven V-band frequencies for 719 clear-sky comparisons at the SGP during 2000-2002.

Frequency, GHz	ΔT_B, K		T_B, K		$\Delta T_B/T_B$
	Mean	Std. Dev.	Mean	Std. Dev.	Std. Dev.
51.25	1.11	1.72	111	6.70	0.015
52.28	-0.86	1.36	153	6.12	0.009
53.85	0.62	0.65	257	5.88	0.003
54.95	-0.07	1.18	287	5.68	0.004
56.66	0.77	0.45	294	6.47	0.002
57.29	1.06	0.47	294	6.51	0.002
58.80	0.86	0.79	295	6.67	0.003

Although the standard deviation of the differences is generally small – mostly less than 1 K and considerably less than 1% of the mean – the 51.25 GHz channel appears to be noisy relative to the other channels, and the 54.94 and 58.80 GHz channels appear to have become

considerably noisier in July 2002. This aspect of radiometer performance is quantified by the

noise figure F in decibels, defined by Solheim (1993) as

$$F = 10\log\left(\frac{T_r + T_0}{T_0}\right).$$ (6)

T_0 is a reference temperature set to 290 K by convention. T_r is the effective noise temperature of

the receiver such that the brightness temperature T_B corresponding to a signal voltage V

measured by the radiometer is given by

$$T_B = G^{-1}(V - V_0)$$ (7)

and V_0 is the voltage offset due to the receiver temperature (i.e., $T_r = G^{-1}V_0$).

Substituting (2) for the gain into (7), T_r can be calculated as

$$T_r = \frac{T_{hi} - Y T_{lo}}{Y - 1},$$ (8)

where $Y = V_{hi}/V_{lo}$. In the case of the MWRP for $T_{lo} = T_{ref}$ and $T_{hi} = T_{ref} + T_{nd}$,

$$T_r = \frac{T_{nd}}{Y - 1} - T_{ref}$$ (9)

and $Y = V_{ref+nd} / V_{ref}$.

Weekly averaged values of F are presented in Figure 11 for the 7 V-band channels during

the SGP deployment in 2001-2002. The error bars indicate twice the standard deviation or 96%

of the range of values. The dashed line indicates the value of F (5.55 dB) corresponding to $T_r =$

750K, a typical value for a radiometer of this design. It is clearly evident that the noise figure

significantly exceeds 5.55 dB for the 51.25 GHz channel whereas all of others have noise figures

at or below 5.55 dB until week 29 (mid-July) of 2002. The relatively greater scatter in the

MWRP–Model comparison at 51.25 GHz in Figure 10 and Table 7 reflects the elevated noise

figure for this channel. At week 29 the average value of F jumps above 5.55 dB at 54.94 GHz,

and the spread of the weekly averages increases markedly at 51.25, 54.49, and 58.80 GHz.

Radiometrics diagnosed this as a failing synthesizer.
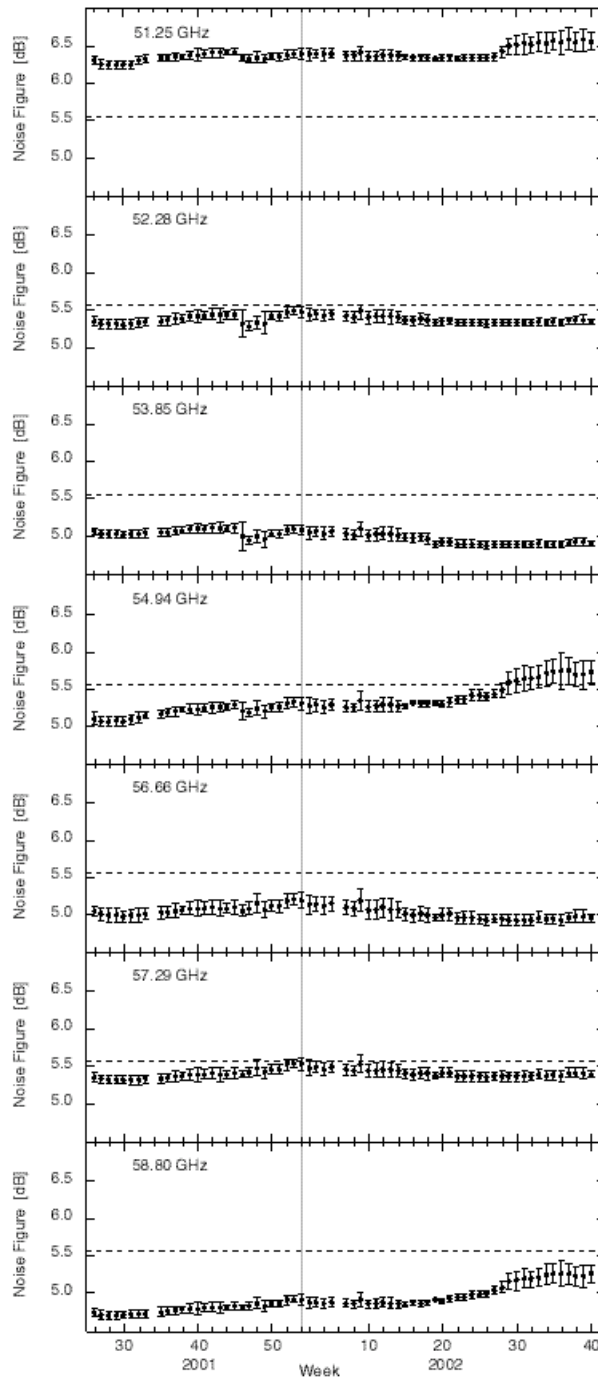
Figure 11. Weekly average values of noise figure for the V-band channels during 2001-2002 at the SGP. The error bars indicate twice the weekly standard deviation. The dotted line corresponds to an effective receiver noise temperature of 750 K.

37

3.3 Infrared Thermometer (IRT)

The accuracy of the IRT measurements was evaluated by comparison with a similar instrument mounted on the collocated MWR at the SGP, and by comparison with the Atmospherically Emitted Radiance Interferometer (AERI) spectrometer at both the SGP and NSA. The comparison with AERI was accomplished by first integrating the AERI spectral radiance $L(v)$ over the IRT pass band $f(v)$

$$L = \int_{v_1}^{v_2} L(v) f(v) \, dv \tag{10}$$

then integrating the Planck radiance $B(v, T)$ over this pass band

$$L^* = \int_{v_1}^{v_2} B(v,T) f(v) \, dv \tag{11}$$

and iteratively adjusting the temperature until $L^* = L$. The results of these comparisons are presented in Figure 12 and summarized in Table 8.

Table 8. Statistical summary of IR temperature comparison (MWRP – MWR) for 2001-2002 at SGP for all sky conditions.

Number of comparisons	19,367
Mean difference (bias)	-0.11 K
Median difference	-0.56 K
Standard deviation	4.5 K

The agreement between the IRT on the MWRP and the IRT on the MWR shows negligible bias. However, the large scatter and corresponding large standard deviation is primarily due to the differences in field of view. The IRT on the MWRP has a 30° field of view whereas the field of view of the IRT on the MWR is less than 3°. Although the larger field of view permits greater sensitivity, it also causes the IRT to respond to clouds that are not within the field of view of the

MWRP (Table 1). The agreement with AERI is also good, but shows increasing bias at low sky temperatures. This is consistent with the expected decrease in accuracy as the difference between the IRT housing temperature and the target temperature increases (Table 1).
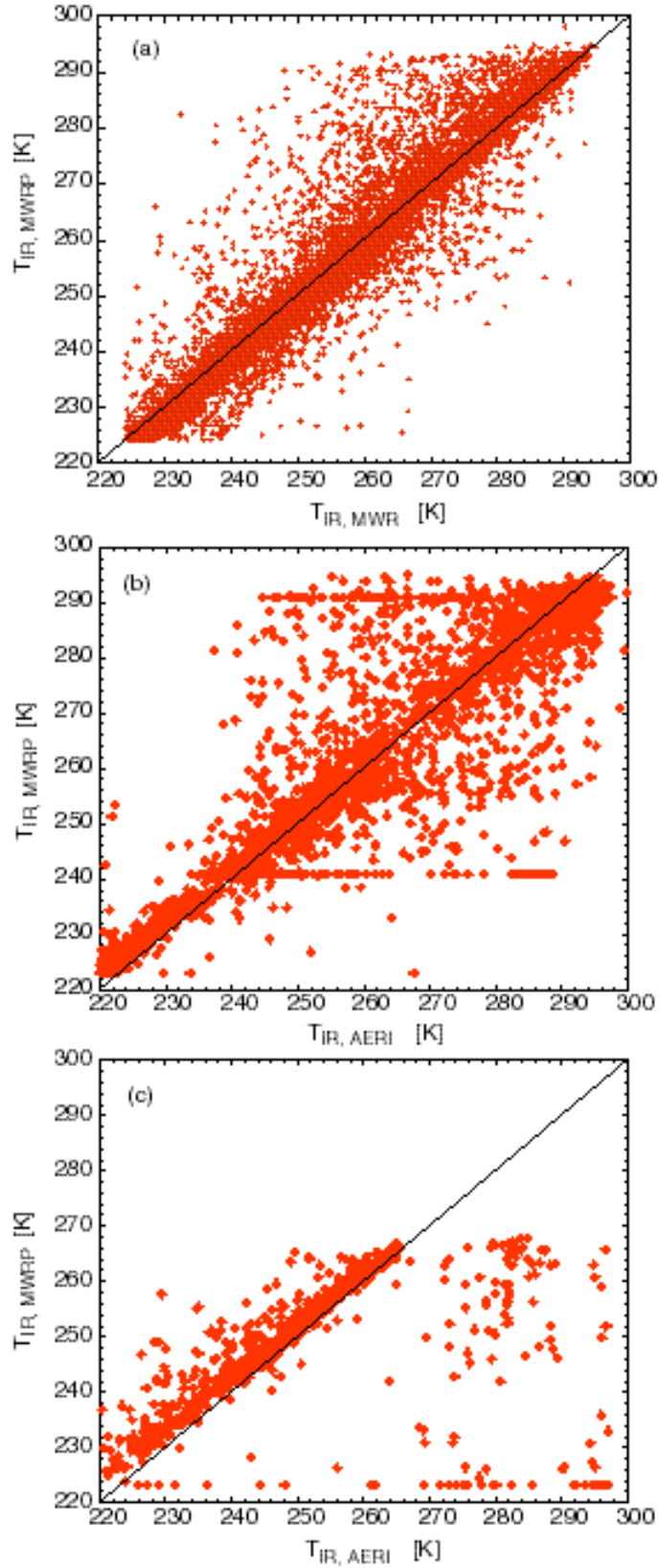
Figure 12. Comparison of IRT on MWRP with (a) IRT on MWR at SGP for 2002-2001; (b) AERI at SGP during June 2001; (c) AERI at NSA during February 2001.

3.4 Surface Meteorological Sensors

The comparison of the barometric pressure, temperature, and relative humidity sensors in the MWRP to the surface values of the radiosondes is summarized in Table 9.

Table 9. Statistical summary of surface meteorological sensor comparison (MWRP – sonde) for 719 soundings at SGP, 2001-2002.

	ΔP, mb	ΔT, K	ΔRH, %
Mean (bias)	-0.14	0.12	-0.48
Standard deviation	0.66	0.71	3.5

These results are consistent with the combined uncertainty in the MWRP sensors and the radiosonde sensors.

4.0 Retrieval Skill

The MWRP uses neural network retrieval algorithms described by Solheim et al. (1998) to derive the vertical profiles of temperature, water vapor density, and cloud liquid water content, as well as the total precipitable water vapor (PWV) and the cloud liquid water path (LWP) from the measured brightness temperatures. These retrievals use the zenith brightness temperatures only; no off-zenith measurements are used to improve the vertical resolution of the retrievals.

The temperature and water vapor profile retrievals are evaluated by comparison with collocated radiosondes (sgpsondewnpnC1.b1). For reference, temperature and water vapor profiles retrieved using the combined Geostationary Operational Environmental Satellite (GOES) and AERI radiances (sgpgaeriprofC1.c1) described by Smith et al. (1999) were also compared with radiosondes. The GOES+AERI retrievals were selected for comparison because

they represent the state-of-the-art for thermodynamic profiling using passive radiometric remote sensors currently available to the ARM Program.

The retrieved profiles of liquid water content (LWC) are evaluated by comparison with LWC profiles derived using the millimeter cloud radar (MMCR) and the two-channel microwave radiometer (MWR). The retrieved PWV and LWP are compared with results from the two-channel MWR.

4.1 Temperature Profile

In Figure 13, the mean (bias) and standard deviation of the temperature differences between the MWRP or GOES+AERI and the radiosondes (i.e., $T_{MWRP} - T_{sonde}$ or $T_{GOES+AERI} - T_{sonde}$) are presented for spring, summer, fall, and winter periods as defined in Table 10. The range of PWV guided the choice of beginning and ending dates for the periods.
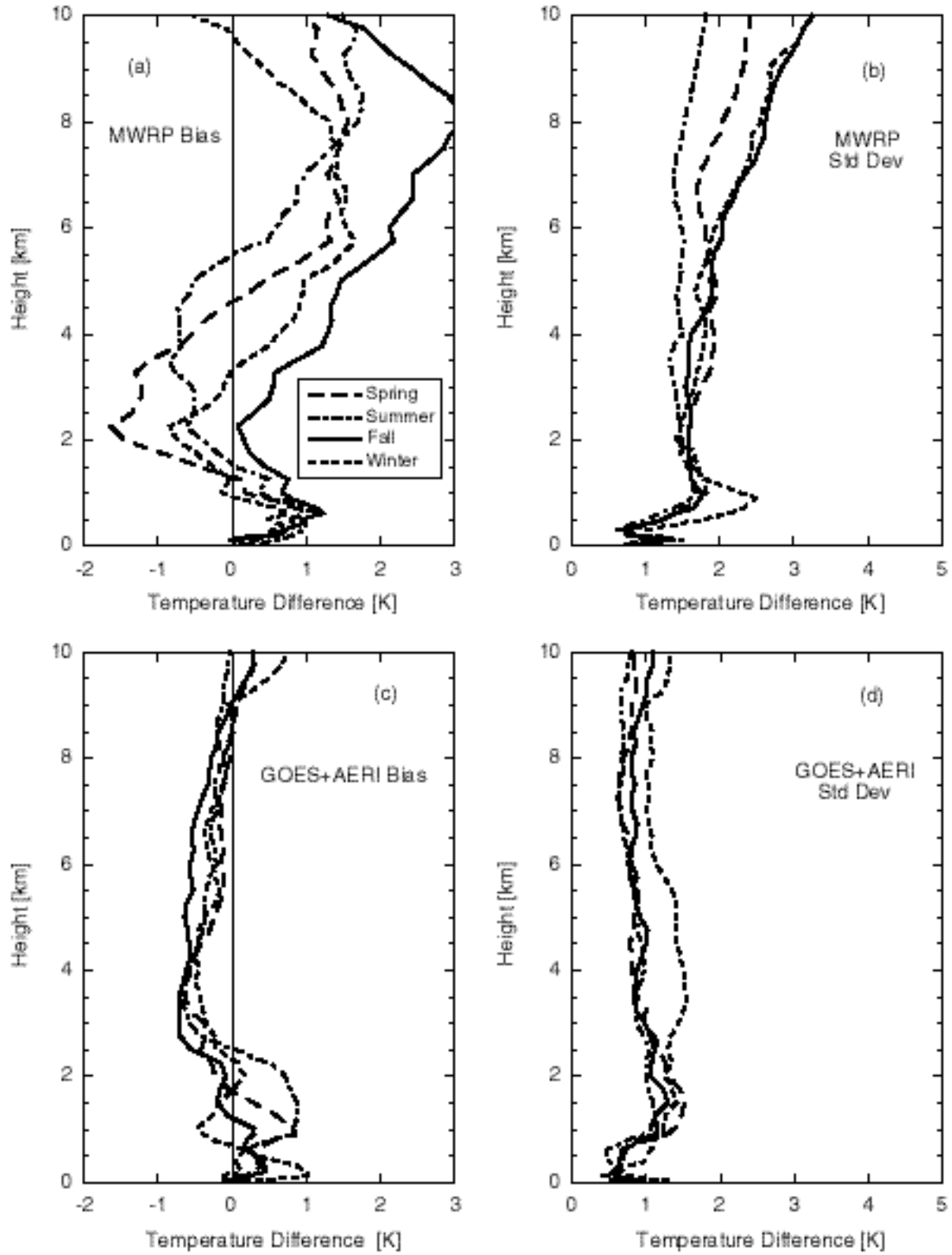
Figure 13. (a) mean (bias) and (b) standard deviation of $T_{MWRP}-T_{sonde}$; (c) mean and (b) standard deviation of $T_{GOES+AERI}-T_{sonde}$ for spring (dashed), summer (dot-dashed), fall (solid), and winter (dotted) periods.

Table 10. Number of radiosonde comparisons for the MWRP and GOES+AERI retrievals.

Period (dates)	MWRP comparisons	GOES+AERI comparisons
Spring (March 15 – June 14, 2002)	290	191
Summer (June 15 – August 30, 2001; June 15 – August 30, 2002)	441	294
Fall (September 1 – December 6, 2001; September 1-30, 2002)	371	188
Winter (December 6, 2001 – March 14, 2002)	142	115

The number of GOES+AERI comparisons is less than the number of MWRP comparisons because the GOES+AERI retrievals are valid only for clear sky conditions whereas the MWRP retrievals are valid for all (non-precipitating) conditions.

It is evident from Figure 13 that a significant bias exists between the temperature profiles from the MWRP and those from the radiosondes. The bias in the GOES+AERI comparisons with radiosondes is much smaller. The seasonal variation in the MWRP bias is also substantial. Because the MWRP retrievals are developed from an ensemble of model-calculated brightness temperatures corresponding to an ensemble of radiosondes, it is likely that the biases evident in Figure 13 arise, at least in part, from the biases between the measured and model-calculated brightness temperatures discussed in the previous section. To assess this possibility, the perturbation in the retrieved temperature profile δT resulting from adding an offset to the brightness temperatures was determined for several situations. The perturbations resulting from adding a 1-K offset to the mean clear sky brightness temperatures during 2000-2002 are shown in Figure 14(a) for the five K-band frequencies and in Figure 14(b) for the seven V-band

frequencies. Although it is not surprising that the contribution of the V-band channels is dominant, with the more opaque channels contributing strongly in the lowest kilometer and the least opaque channels contributing over a broad range of altitudes, it is interesting that the K-band channels have a significant contribution above 6 km. To be more realistic, the perturbation in the retrieved temperature profile due to adding the mean measured–modeled brightness temperature differences during the summer to the mean summer brightness temperatures is presented in Figure 14(c) for the K-band channels (dashed line), V-band channels (dotted line), and all channels (solid line). Evidently, the significant difference between the measured and modeled brightness temperatures at 22.235 GHz due to the line width being too large can cause ~1 K bias in the temperature retrieval in the upper troposphere. In addition, the ~1 K offset between the measured and modeled brightness temperatures at 56.66, 57.29, and 58.80 GHz during the summer evident in Figure 10 can cause a positive bias in the temperature retrieval below 1 km and a negative bias above 1 km.

Figure 14(d) shows the temperature perturbations from all frequencies for spring (dashed), summer (dot-dashed), fall (solid), and winter (dotted) due to the mean measured-modeled brightness temperature offsets in those periods. The ~1 K profile bias above 6 km during the fall is a direct result of the biases at 52.28 and 53.85 GHz during the fall apparent in Figure 10; the bias in the fall profile would have been even larger except for the negative contribution to the profile error due to the positive bias in at 51.25 GHz during the fall.
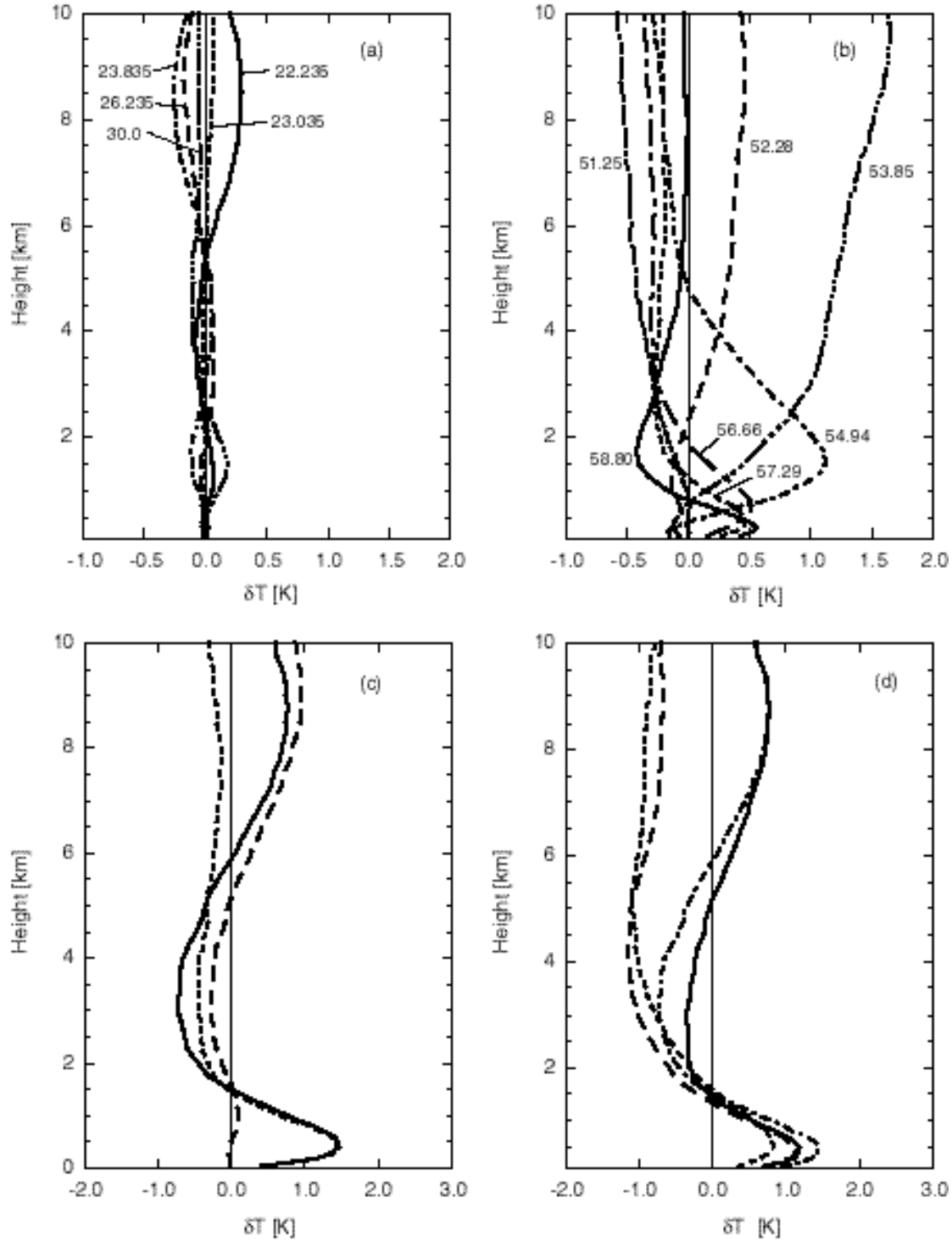
Figure 14. Perturbations in the retrieved temperature profile δT due to (a) adding a 1-K offset to the mean K-band brightness temperatures for clear sky conditions during 2000-2002; (b) same as (a) but for the V-band; (c) adding mean measured-modeled brightness temperature offsets during the summer for K-band (dashed), V-band (dotted), and all (solid) measurement frequencies; (d) adding mean brightness temperature offsets at all frequencies for spring (dashed), summer (dot-dashed), fall (solid), and winter (dotted).

Comparing the results of Figure 14(d) with Figure 13(a), it is apparent that the brightness temperature offsets can explain much of the observed bias in the temperature profile retrieval, especially in the lower troposphere. At greater altitudes the observed spring and winter profile biases in Figure 13(a) are positive whereas the biases suggested by Figure 14(d) are negative. This indicates that other factors, such as vertical resolution, affect the observed bias also.

To provide a quantitative measure of the retrieval skill, a skill coefficient $S(z)$ is defined by analogy with the correlation coefficient of linear regression:

$$S^2(z) = 1 - \left(\frac{MSQ[T(z) - T_{sonde}(z)]}{Var[T_{sonde}(z)]} \right) \tag{12}$$

where $MSQ[\bullet]$ indicates the mean square, $Var[\bullet]$ indicates the variance, $T(z)$ is the retrieved temperature profile, and $T_{sonde}(z)$ is the radiosonde profile. A value of $S = 1$ indicates that the retrieval explains all of the observed variance in the radiosonde profiles (perfect skill); a value of $S = 0$ indicates that the retrieval explains none of the observed variance (no skill). In Figure 15 the skill coefficient profiles for temperature are presented for (a) the MWRP, (b) the MWRP with the bias removed, i.e., using $Var[T-T_{sonde}]$ instead of $MSQ[T-T_{sonde}]$ in (12), and (d) GOES+AERI during the spring (dashed), summer (dot-dashed), fall (solid), and winter (dotted). The standard deviation of the radiosonde temperature profiles about the mean for each period is provided in Figure 15(c). The GOES+AERI skill is quite good during the spring, fall, and winter; the reduced summer skill is due to the smaller standard deviation of the radiosonde profiles during the summer. Removing the bias from the MWRP more accurately portrays the skill of the neural network retrieval; nevertheless it remains inferior to the GOES+AERI skill, especially in the upper troposphere where the benefit of the GOES contribution is obvious.

47
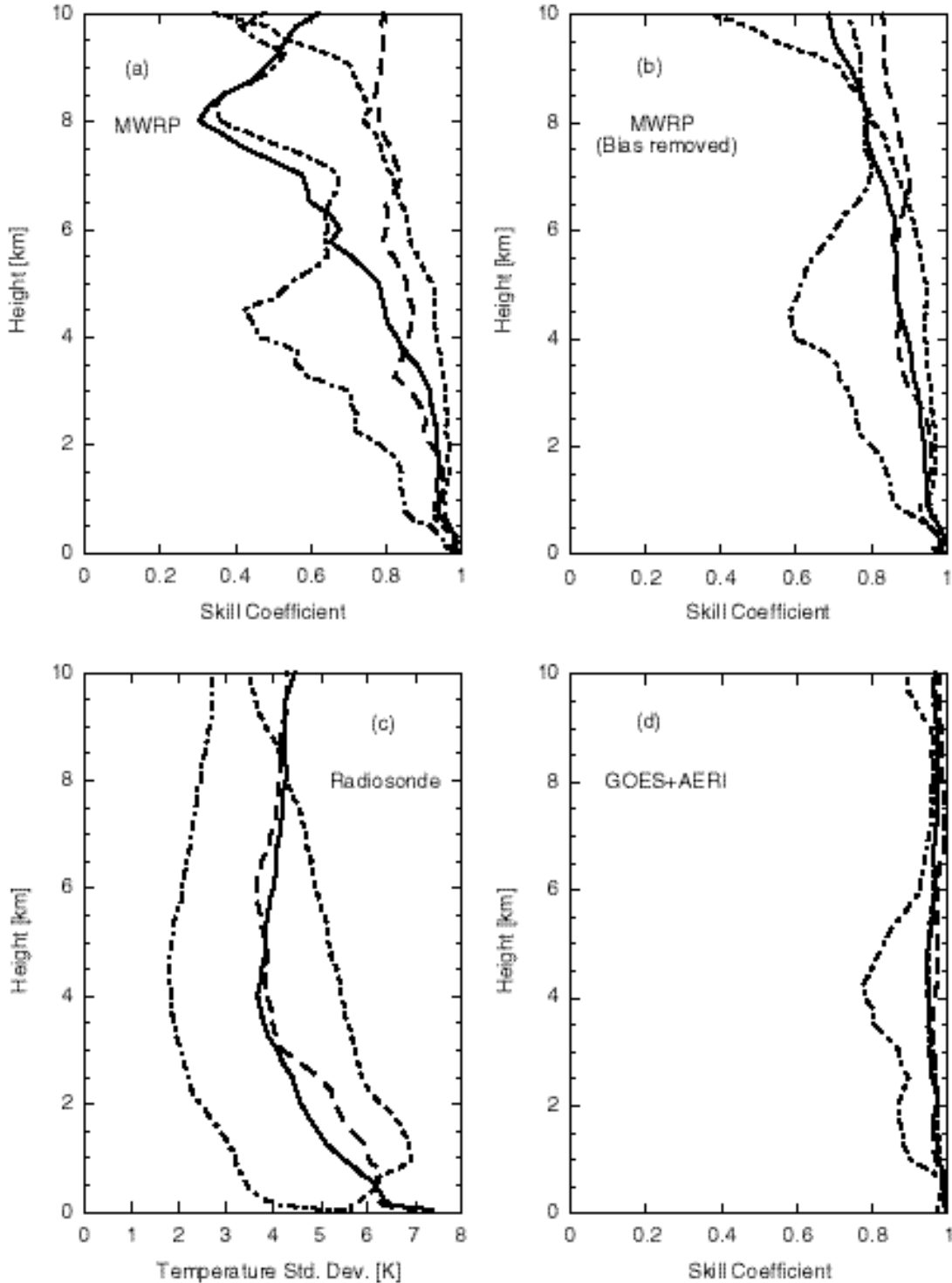
Figure 15. Temperature retrieval skill coefficient profiles for (a) MWRP, (b) MWRP with the bias removed, and (d) GOES+AERI during the spring (dashed), summer (dot-dashed), fall (solid), and winter (dotted). The standard deviation of the radiosonde temperature profiles based on the number of observations in the MWRP comparison (see Table 10) for each period is shown in (c); the radiosonde standard deviations for the reduced sets corresponding to the GOES+AERI observations during these periods are slightly smaller.

4.2 Water Vapor Density Profile

In Figure 16, the mean (bias) and standard deviation of the water vapor density differences between the MWRP or GOES+AERI and the radiosondes (i.e., $\rho_{MWRP} - \rho_{sonde}$ or $\rho_{GOES+AERI} - \rho_{sonde}$) are presented for spring, summer, fall, and winter periods as defined in Table 8. The MWRP retrievals exhibit a significant negative bias that peaks near 1 km, then a substantial positive bias at 3-6 km, especially during the summer. GOES+AERI also exhibits a significant negative bias during the summer (dot-dashed) near 1 km. This may arise in part from sharp gradients at the top of the boundary layer that neither passive profiler can completely resolve. The MWRP and GOES+AERI standard deviations are qualitatively similar; the MWRP values are generally larger because they are computed for a much larger number of observations spanning both clear and cloudy conditions.

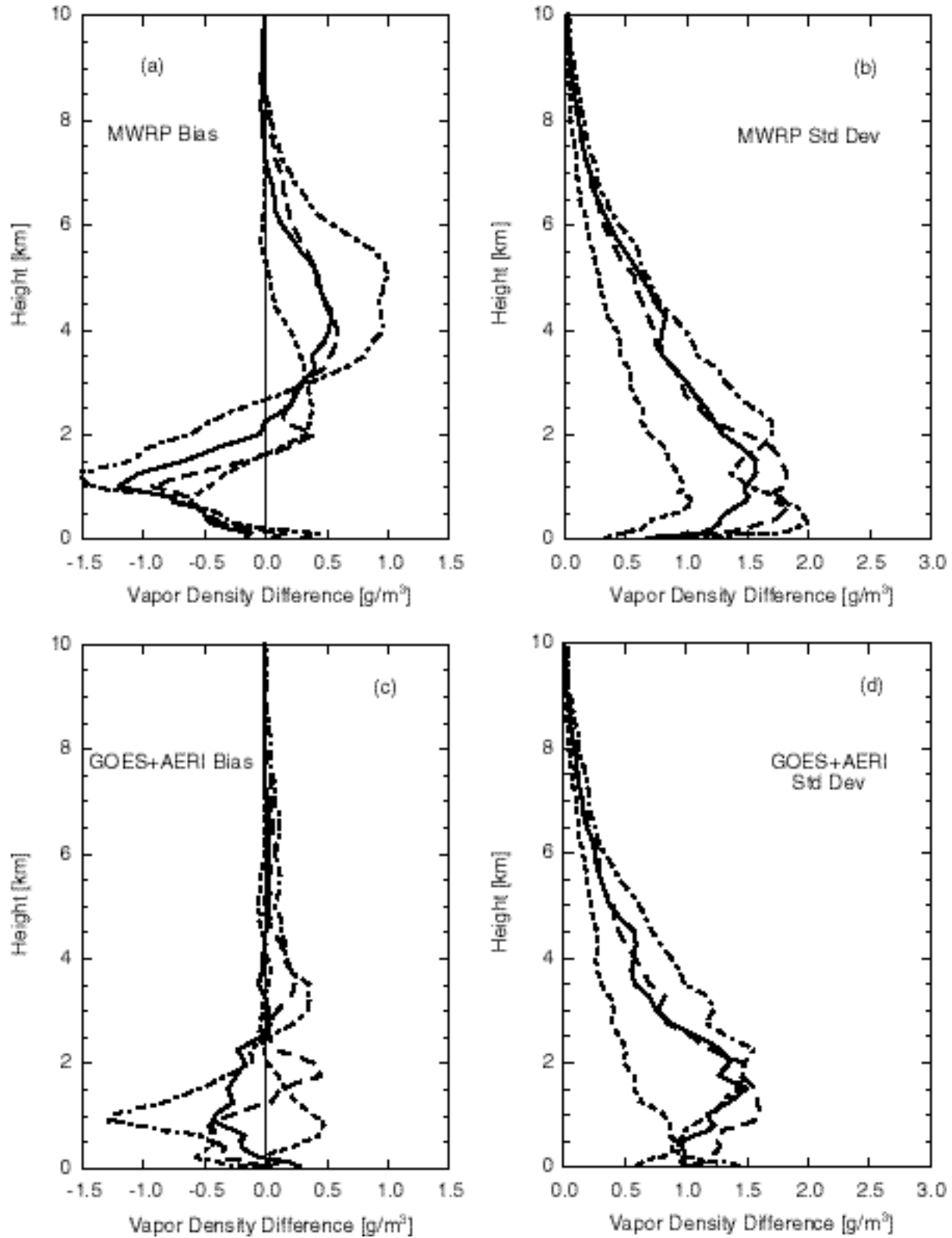**Figure 16.** (a) mean (bias) and (b) standard deviation of $\rho_{MWRP}-\rho_{sonde}$; (c) mean and (b) standard deviation of $\rho_{GOES+AERI}-\rho_{sonde}$ for spring (dashed), summer (dot-dashed), fall (solid), and winter (dotted) periods.

50

To assess the effect of measured-modeled brightness temperature offsets on the retrieved vapor density profiles, the perturbation $\delta\rho$ in the retrieved profile due to brightness temperature offsets were computed as discussed earlier for the temperature perturbations. Figure 17(a) and (b) show that although the K-band perturbations dominate at most altitudes, near the surface the V-band perturbations are more significant (for equal 1-K brightness temperature offsets). For the mean measured-modeled brightness temperature offsets observed during the summer, Figure 17(c) confirms that the V-band perturbations (dotted) are significant near the ground, and that the shape of the perturbation from all frequencies (solid) is qualitatively consistent with the observed summer bias in Figure 16(a). Indeed, the perturbations for all four seasons are consistent with the seasonal trends in Figure 16(a). It is likely that the observed biases in the MWRP density retrieval are due in large part to the width parameter of the 22.235 GHz water vapor line being about 5% too large.
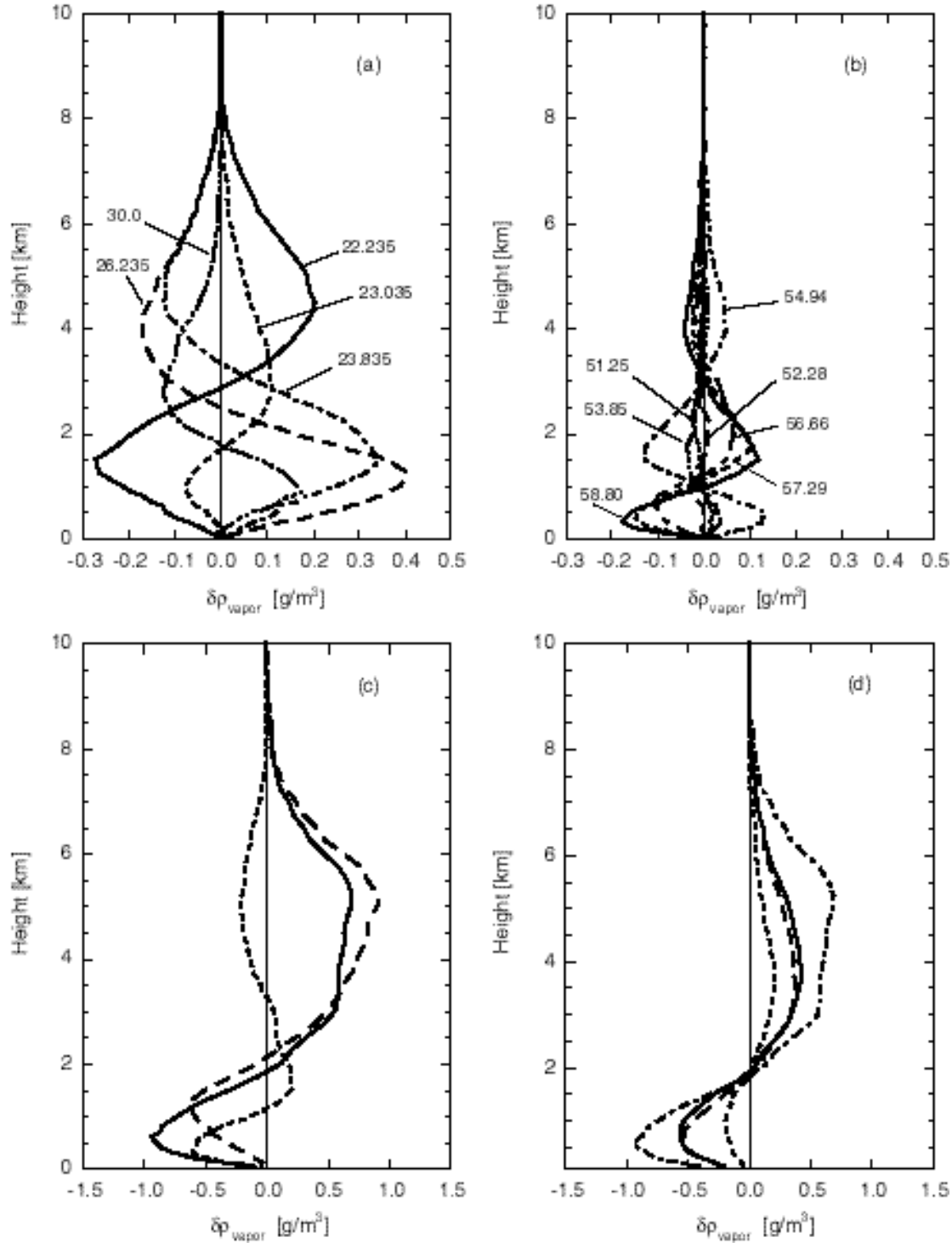
Figure 17. Perturbations in the retrieved vapor density profile $\delta\rho$ due to (a) adding a 1-K offset to the mean K-band brightness temperatures for clear sky conditions during 2000-2002; (b) same as (a) but for the V-band; (c) adding mean measured-modeled brightness temperature offsets during the summer for K-band (dashed), V-band (dotted), and all (solid) measurement frequencies; (d) adding mean brightness temperature offsets at all frequencies for spring (dashed), summer (dot-dashed), fall (solid), and winter (dotted).

52

The skill coefficients for the vapor density retrievals were computed by analogy to (10) and are presented in Figure 18. After removing the bias, the MWRP vapor density retrieval skill generally compares well with GOES+AERI, although there are instances where the observed standard deviation in the MWRP–sonde and AERI+GOES–sonde comparisons equal or exceed the observed standard deviation in the vapor density from the radiosonde, which causes their skill coefficient to fall to zero. Unlike temperature, the mean and standard deviation of the ensemble of water vapor profiles declines exponentially with height, which causes the skill coefficient to become increasingly sensitive to small (absolute) errors with increasing height.
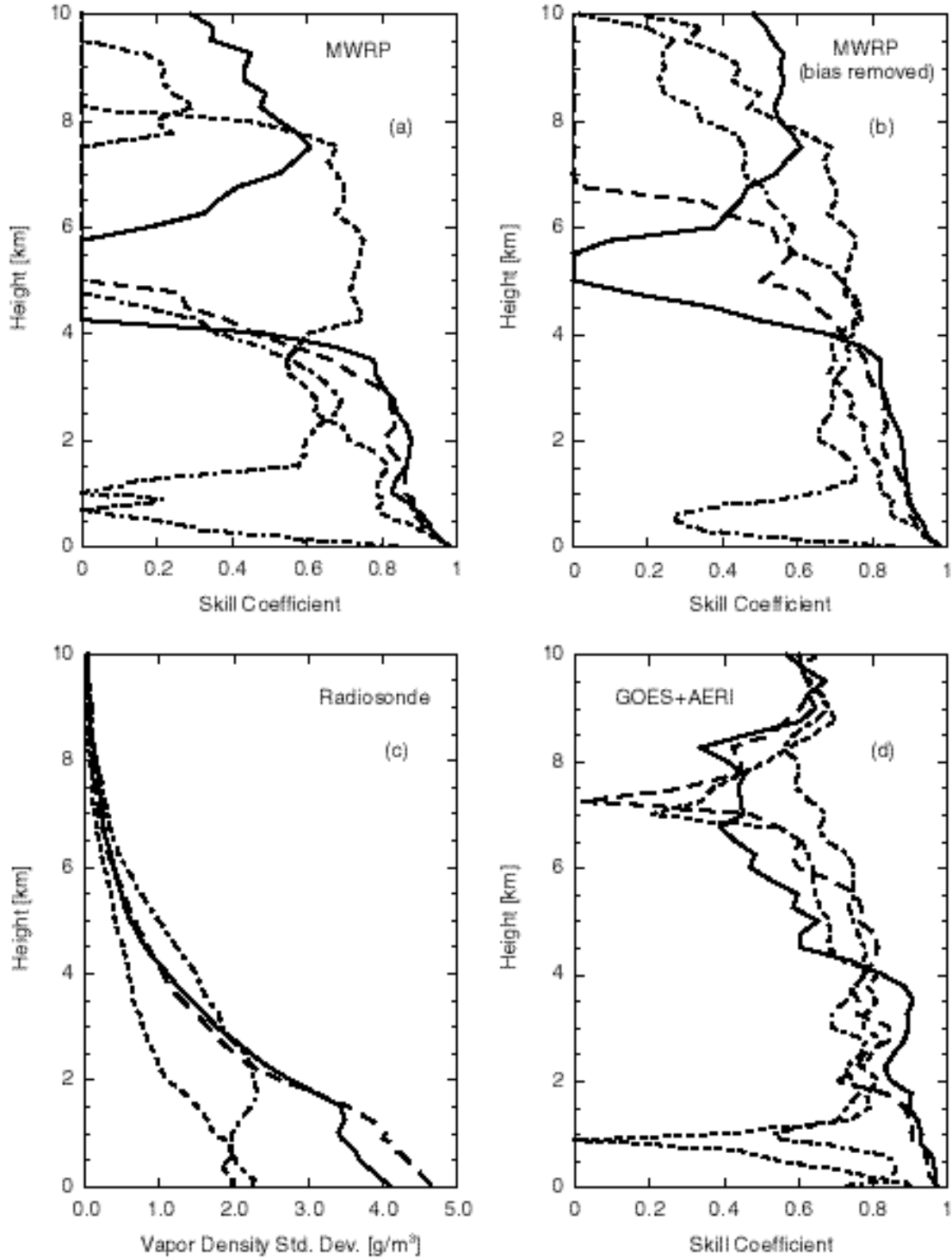
Figure 18. Vapor density retrieval skill coefficient profiles for (a) MWRP, (b) MWRP with the bias removed, and (d) GOES+AERI during the spring (dashed), summer (dot-dashed), fall (solid), and winter (dotted). The standard deviation of the radiosonde vapor density profiles based on the number of observations in the MWRP comparison (see Table 10) for each period is shown in (c); the radiosonde standard deviations for the reduced sets corresponding to the GOES+AERI observations during these periods are slightly smaller.

4.3 Temperature and Water Vapor Profile Vertical Resolution

The vertical resolution of the retrieved temperature and water vapor profiles from the MWRP was determined following Smith et al. (1999) based on the inter-level error covariance $C(z_0,z)$ defined for temperature as

$$C(z_0,z) = \frac{\sum\left[T(z_0) - T_{sonde}(z_0)\right]\left[T(z) - T_{sonde}(z)\right]}{\sqrt{\sum\left[T(z_0) - T_{sonde}(z_0)\right]^2 \sum\left[T(z) - T_{sonde}(z)\right]^2}} \tag{13}$$

where z_0 is the height for which the resolution is to be determined, T is the retrieved temperature, T_{osnde} is the temperature measured by the radiosonde, and the summations are over all of the profiles in the ensemble. Noting that $C(z_0,z=z_0) = 1$, the resolution at z_0 is defined as the distance between the heights z where $C = 0.5$. In Figure 19 the temperature and water vapor density resolution is presented as functions of height for both the MWRP and GOES+AERI. The GOES+AERI results are in good agreement with those presented by Smith et al. (1999). The MWRP results are in good agreement with those presented by Güldner and Spanküch (2001).

The temperature resolution of both the MWRP and GOES+AERI retrievals increase approximately linearly with height up to about 4 km, at which point the GOES+AERI resolution is constant at about 2 km while the MWRP resolution continues to increase. This clearly demonstrates the benefit of using ground-based and satellite-based remote sensors in combination.

The water vapor density resolution of both the MWRP and GOES+AERI retrievals are qualitatively similar up to about 3 km, at which point the MWRP resolution degrades rapidly but then begins to improve at 5 km until it matches the GOES+AERI resolution at about 8 km. Again, the benefit of combining ground- and satellite-based remote sensors is clear.
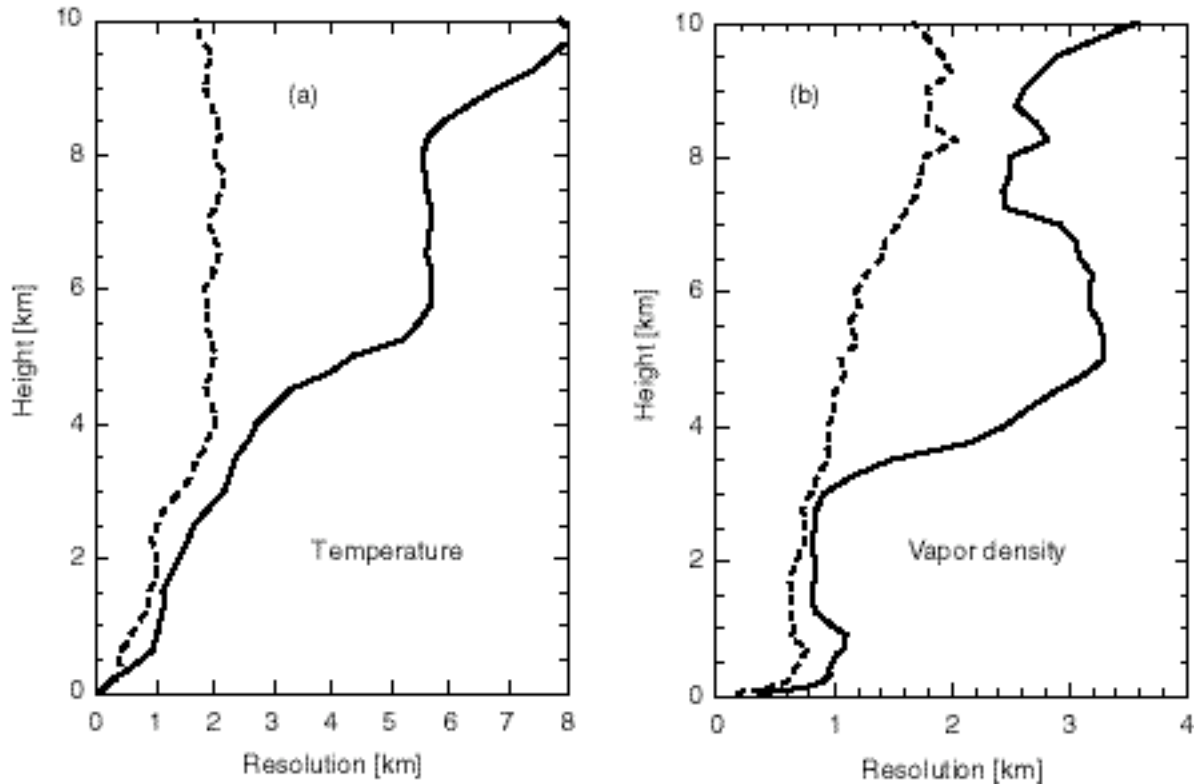
Figure 19. Vertical resolution of the retrieved profiles of (a) temperature and (b) water vapor density for MWRP (solid line) and GOES+AERI (broken line).

The MWRP temperature and water vapor density retrievals rely on zenith measurements of brightness temperature alone. If off-zenith measurements were included in the retrieval, it is possible that the vertical resolution could be improved (Gary, 1988).

4.4 Examples of Temperature and Water Vapor Profiles

Typical profiles of temperature and water vapor from the MWRP are compared in Figure 20 for the SGP and in Figure 21 for the NSA. The results are consistent with the biases presented earlier based on statistical comparisons of the MWRP and radiosondes. Although the surface temperature inversion is accurately reported, the elevated temperature inversions are not. Similarly, the sharp water vapor gradients are substantially smoothed. The question, however, is how well would these features be represented by a SCM or CRM?

56
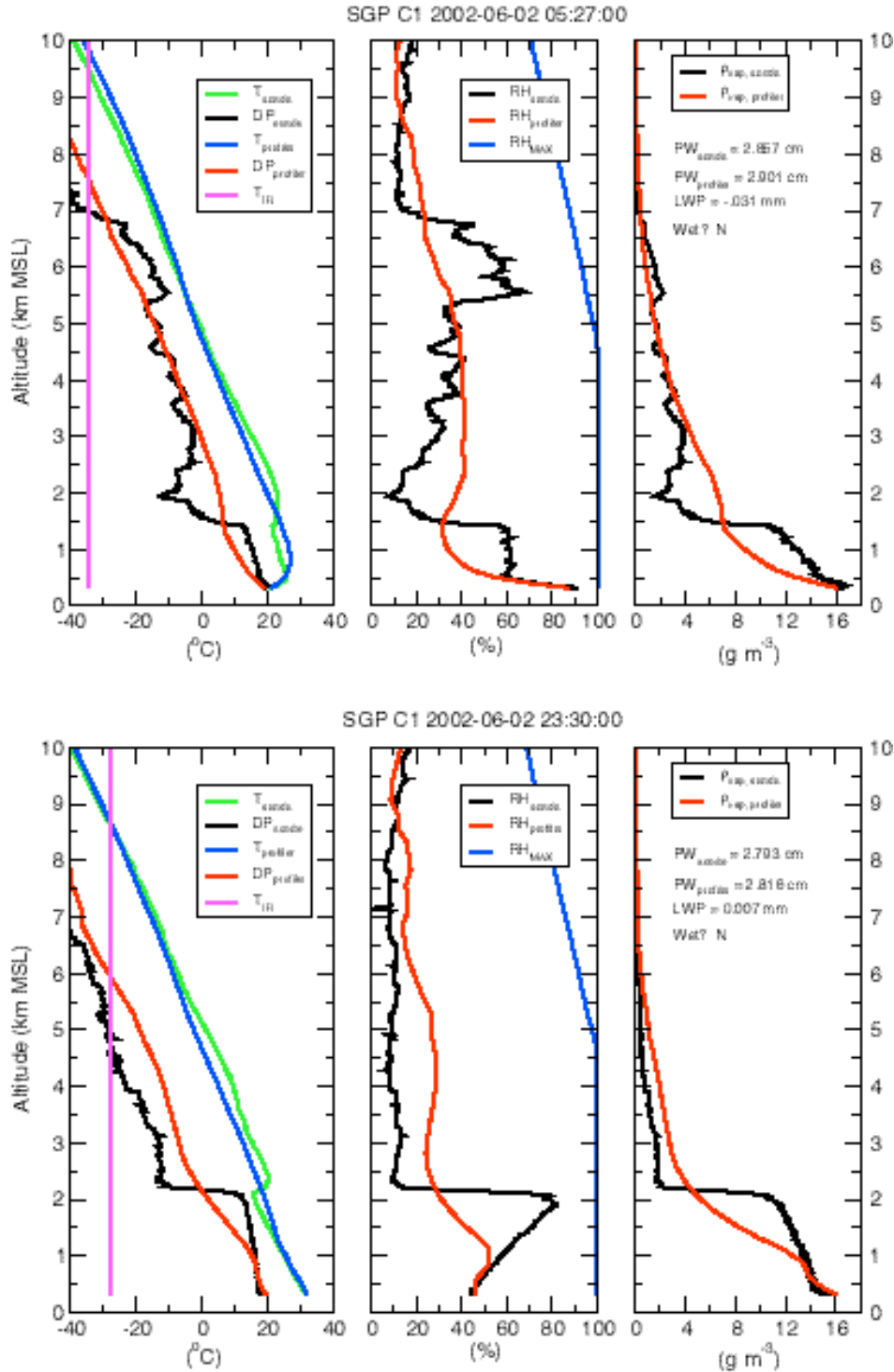
Figure 20. Comparison of temperature and water vapor profiles from the MWRP and radiosonde for 05:27 UTC (23:27 LST) and 23:30 UTC (17:30 LST) on 2 June 2002 at the SGP. RH_{MAX} is100% for temperatures greater than 0 °C; for temperatures less than 0 °C, it is the ratio of the saturation vapor pressure over ice to the saturation vapor pressure over liquid water. T_{IR} is the temperature reported by the infrared thermometer. The altitude at the surface is 317 m above sea level.
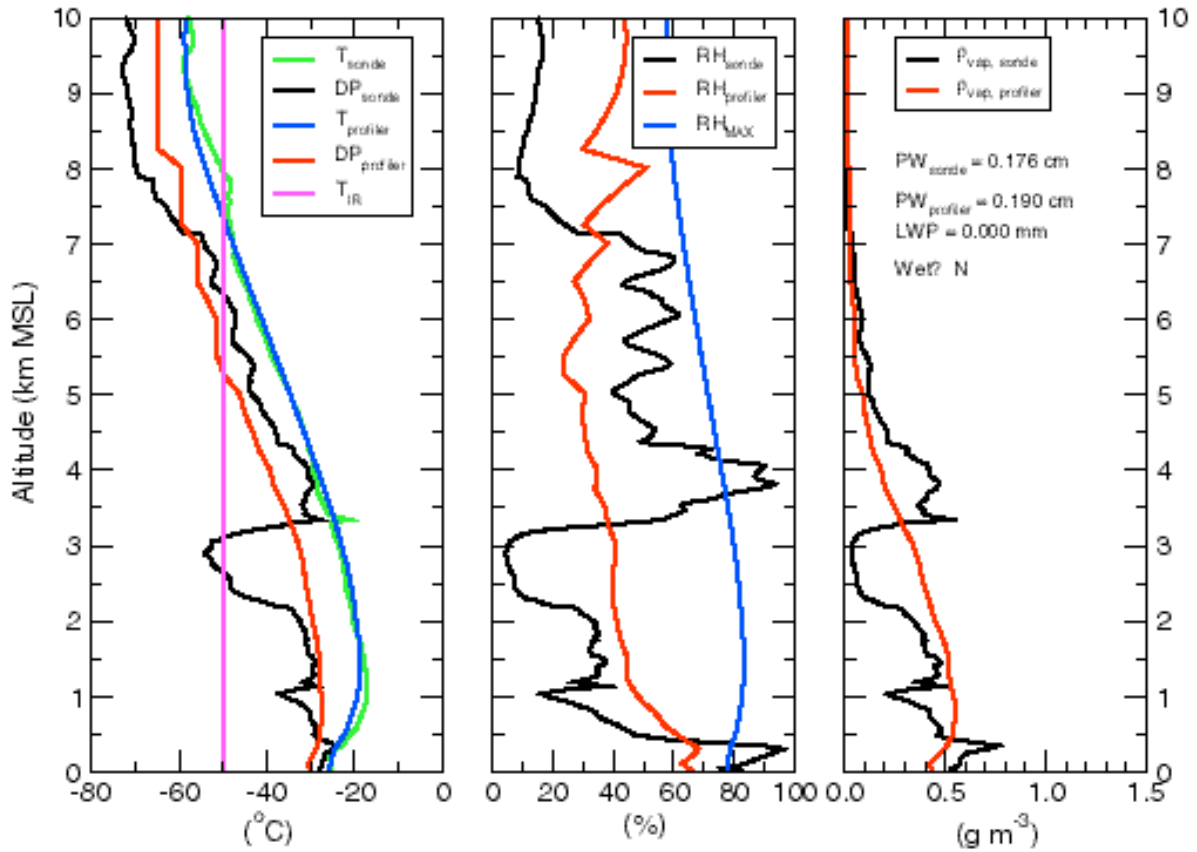
Figure 21. Comparison of temperature and water vapor profiles from the MWRP and radiosonde for very cold, dry conditions at 23:32 UTC on 29 December 2000 at Barrow, Alaska during the polar night.

4.5 Liquid Water Content Profiles

To evaluate the retrieved profiles of liquid water content (LWC) in units of g/m^3 from the MWRP, the reflectivity profiles Z from the millimeter cloud radar (MMCR) at the SGP were scaled with the liquid water path (LWP) in units of g/m^2 as suggested by Frisch et al. (1998)

$$LWC(z_i) = Z_i^{1/2} \frac{LWP}{\Delta z \sum Z_i^{1/2}} \tag{14}$$

where z_i is the height of the ith radar range gate, Z_i is the reflectivity for the ith range gate, Δz is the range gate spacing (30 m), and the summation is over all range gates.

Figure 22 presents histograms of the height of the maximum LWC for both the MWRP and MCMR binned in 250 m intervals. Although the distribution of heights from the MMCR is relatively uniform, the MWRP retrieval tends to place the maximum in the lowest 1 km with a secondary grouping between 4 and 5 km.
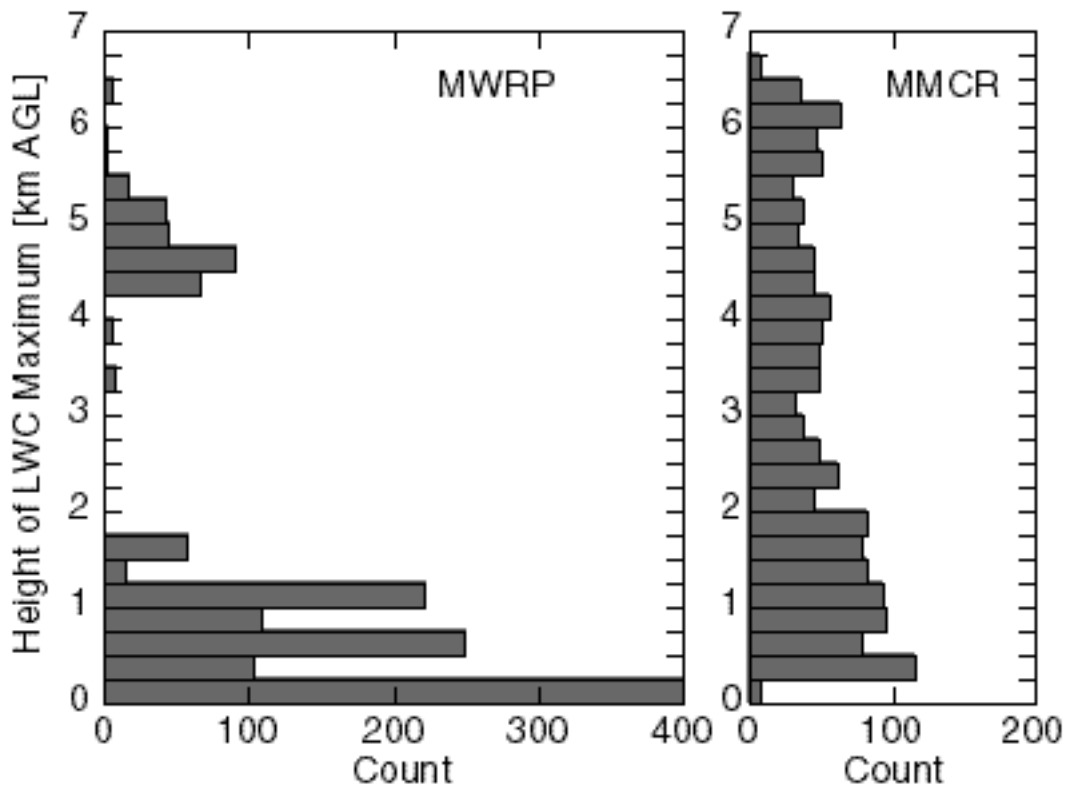
Figure 22. Histograms of the height at which the maximum liquid water content (LWC) was reported by the MWRP and MMCR.

Examples of the LWC profiles from the MWRP and MMCR are given in Figure 23. Clearly there are times when the MWRP and MMCR are in good agreement; more often, however, the MWRP LWC retrieval is not able to even come close to the correct profile. These problems are largely due to limited resolution, but they are exacerbated by an ambiguity in cloud base height inferred from the cloud base temperature measured with the IRT when a temperature inversion situation exists.
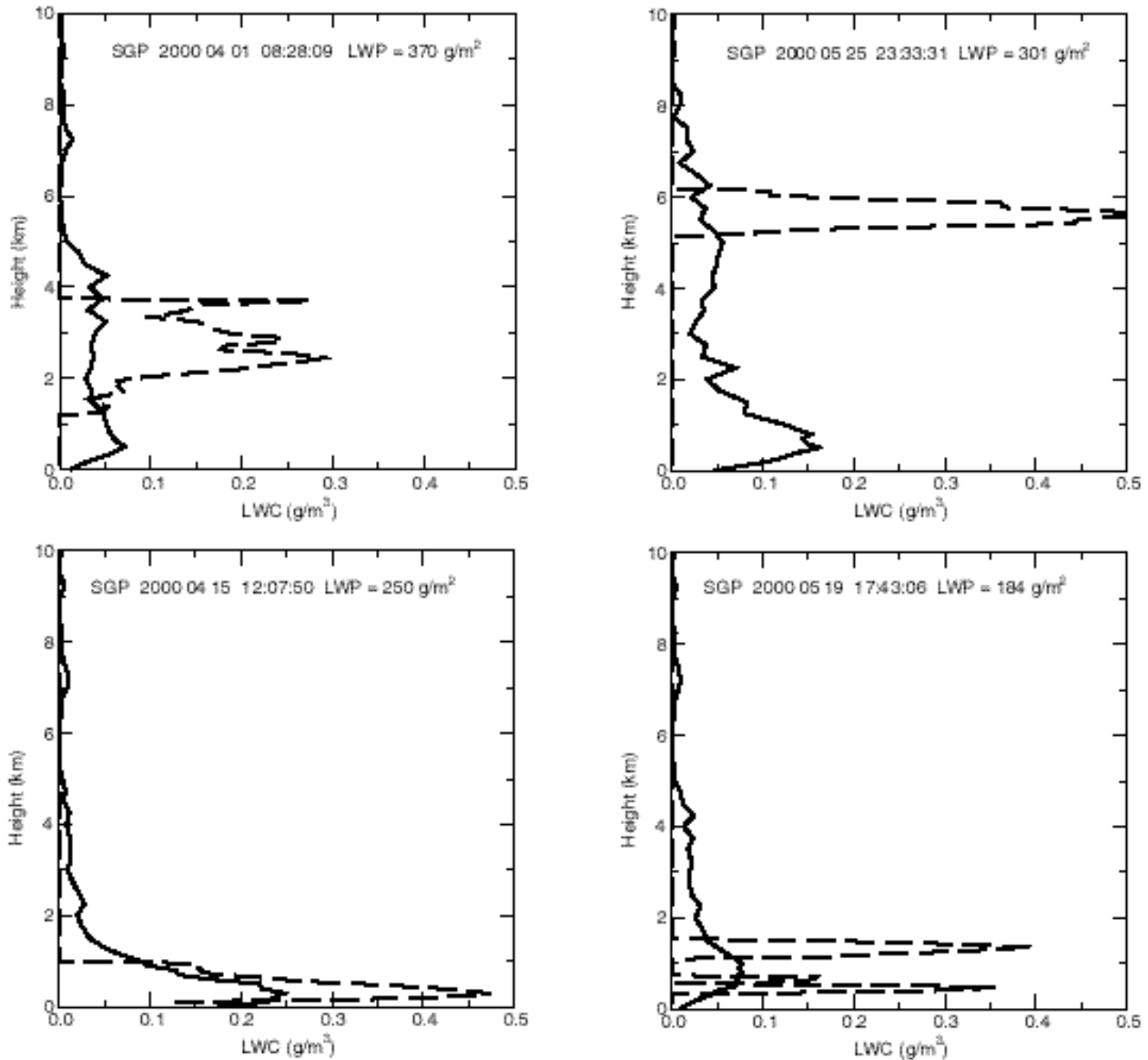
Figure 23. Vertical profiles of liquid water content derived from the MWRP (solid) and MMCR (broken).

4.6 Precipitable Water and Liquid Water Path

The comparison of the precipitable water vapor (PWV) and liquid water path (LWP) derived from the MWRP with values derived from the two-channel MWR are presented in Figure 24 and summarized in Table 11. For the PWV, the comparison is for January-September 2002; LWP the comparison is for 15 April-September 2002. (On 15 April 2002 new retrieval

coefficients were installed on the MWR that were based on the same absorption models used to derive the MWRP retrievals. The effect on retrieved PWV is not discernable, but the retrieved LWP is 10-30% less using the new retrieval.) The trend in PWV differences follows the trend of the brightness temperature differences at 23.8 GHz presented in Figure 6. The LWP comparison shows good agreement between the two retrievals for LWP less than 0.1 mm. The increasing difference at large values of LWP reflects the impact of the additional temperature-sensing channels of the MWRP to provide information on the temperature of the liquid water, which the two-channel MWR is not able to provide (Liljegren et al., 2001).

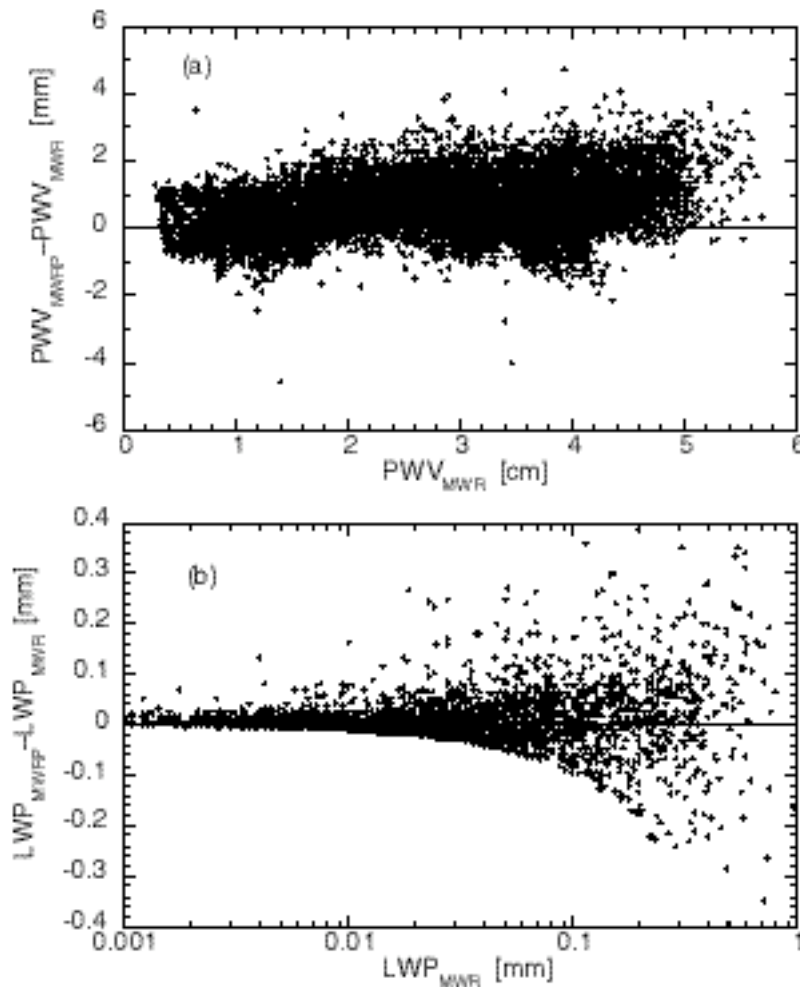
Figure 24. Differences in (a) precipitable water vapor (PWV) and (b) liquid water path (LWP) derived from the MWRP and two-channel MWR. The PWV comparison is for January-

September 2002; the LWP comparison is for 15 April-September 2002 due to the significant change in the MWR LWP retrieval on 15 April 2002.

Table 11. Summary of MWRP–MWR comparison of PWV and LWP.

	Number	Mean, mm	Median, mm	Std Dev, mm	RMS, mm
ΔPWV (all)	13,689	0.66	0.66	0.77	1.01
ΔLWP					
(cloudy)	3356	0.010	0.002	0.064	0.065
(LWP < 0.1 mm)	2495	0	0	0.023	0.023
(clear)	11,118	-0.013	-0.013	0.023	0.026

5.0 Conclusions and Recommendations

5.1 Hardware

The MWRP has proven to be robust, operating continuously and successfully for extended periods in the extreme cold of the polar winter and the extreme heat of three Oklahoma summers. The need to replace the tunable frequency synthesizer twice after each year of operation is attributed to the use of the "first generation" version of the synthesizer in this early version of the MWRP (serial number 002). The newly installed synthesizer is a "third generation" version that is expected to be more reliable. Routine monitoring of the radiometer's performance through the receiver noise figure is advisable.

5.2 Accuracy and Calibration

The calibration of K-band (vapor sensing) channels appears to be quite stable, and in reasonable agreement with the liquid nitrogen calibration checks. The comparisons with the brightness temperatures measured with a collocated two-channel MWR agree to about the

claimed accuracy despite an unexplained systematic trend in the differences. A more in-depth analysis of the calibration algorithms is probably warranted to try to identify the source of this systematic behavior. Comparison with model-calculated brightness temperatures reveals that the line width parameter of the 22.235 GHz water vapor line is about 5% too large.

The calibration of the V-band (temperature sensing) channels on a semi-annual schedule appears sufficient, although routine monitoring of the brightness temperatures is advisable to identify unusual calibration drifts in a particular channel or two that may require more frequent calibration. Comparison with model-calculated brightness temperatures indicates persistent biases of 1-2 K, which may reveal the limit of the LN_2 calibration accuracy or the limit of the oxygen absorption model accuracy.

The infrared thermometer and meteorological sensors appear to be accurate to within their claimed accuracy. It would be preferable to replace the wide (30°) field of view lens of the IRT with the narrower field of view lens used by ARM so that it more nearly matches the field of view of the MWRP.

5.3 Retrieval Skill

The vertical temperature and water vapor profiles derived from the MWRP brightness temperatures using the vendor-supplied neural network retrievals compare reasonably well with radiosonde soundings, typically exhibiting maximum root-mean-square, i.e., $(bias^2 + standard\ deviation^2)^{1/2}$, differences of 2 °C for temperature and 2 g/m^3 for water vapor. In comparison with profiles retrieved from GOES+AERI, it is obvious that the MWRP retrievals exhibit significantly greater bias. These biases are due in part to biases between the modeled and measured brightness temperatures that arise due to problems with the models. Facing a similar bias problem, Smith et al. (1999) constructed a "bias spectrum" based on observed

measured–modeled differences, which is applied to the measurements prior to the retrieval. If such a bias spectrum were developed for the MWRP (or the model errors corrected), then the retrieval biases would be substantially reduced and the skill coefficients of the temperature and water vapor profiles would be more nearly comparable to GOES+AERI, though still not quite as good. However, this may be an acceptable trade-off for the all weather capability of the MWRP.

It is clear that the vertical resolution of the MWRP temperature and water vapor profiles is much coarser than the radiosondes – as discussed in the Introduction, the MWRP offers much improved temporal resolution at the expense of decreased vertical resolution; however, it is more in line with the temporal and vertical resolution of the single-column and cloud-resolving models. Still, the observed biases are due in part to the inability of the MWRP to resolve elevated temperature inversions and sharp water vapor gradients. The degree to which incorporating off-zenith measurements in the retrieval would improve the vertical resolution should be investigated. Also, the vertical resolution of the GOES+AERI combination is clearly superior, especially in the upper troposphere. Combining the MWRP with GOES or other satellite-based sounding instrument would similarly improve the upper tropospheric performance.

The current observing cycle requires about 15 min to complete, in part because an angular scan of the sky is performed each cycle to support tipping curve calculations, and in part because redundant measurements are acquired. Eliminating redundant measurements and maing better use of the angular scans (i.e. extracting the zenith measurements from the scan rather than making separate zenith measurements) would permit the observing cycle to be shortened. Not only would this improve the temporal resolution, but it would reduce the possibility that the sky

conditions could change between measurements at different frequencies during the same observing cycle, thereby improving the achieved skill of the retrievals.

The liquid water content retrieval needs improvement. As it currently exists it cannot consistently locate the height of the maximum liquid water content with demonstrable skill. If the MWRP were to be combined with a ceilometer for true cloud base height, rather than rely on the IRT cloud base temperature to infer cloud base height from the temperature profile (which can be affected by temperature inversions), the liquid water content profiling would probably show more skill. It is also possible that an iterative physical retrieval approach such as Smith et al. (1999) have developed for GOES+AERI might be more successful than the neural network approach, not just for liquid water content profiling but for temperature and water vapor as well.

The precipitable water vapor retrievals compare well with the MWR results, but the differences between the MWRP and MWR exhibit a trend that mirrors the trend in the brightness temperature differences. The liquid water path retrieval is probably more accurate than that for the MWR because of the additional constraint provided by the temperature-sensitive V-band channels.

5.4 Summary

The MWRP, while not quite perfect, offers significant potential to meet the needs of the ARM Program for routine, autonomous profiling of temperature and water vapor with high reliability, high stability, and high temporal resolution. The trade-off is coarser vertical resolution than the radiosonde. The question of whether this is suitable for use in SCMs and CRMs is still unresolved and will only be resolved by making the MWRP data routinely available to the modeling community.

Based on this evaluation, it is recommended that the ARM Program incorporate the MWRP into its existing complement of remote sensors for deployment at each of the four SGP boundary facilities. It is further recommended that a version of the MWRP that has been additionally hardened for military use be deployed at the NSA central facility at Barrow, Alaska to augment the single radiosonde launched daily, Monday-Friday.

6.0 Literature Cited

Frisch, A. S., G. Feingold, C. W. Fairall, T. Uttal, and J. B. Snider, On cloud radar and microwave radiometer measurements of stratus cloud liquid water profiles. *J. Geophys. Res.*, **103**, 23,195-23,197, 1998.

Gary, B. L., Passive microwave temperature profiler, report JPL-D-5484, Jet Propulsion Laboratory, California Institute of Technology, 25 pp., 1988.

Ghan, S., D. Randall, K.-M. Xu, R. Cederwall, D. Cripe, J. Hack, S. Iacobellis, S. Klein, S. Krueger, U. Lohmann, J. Pedretti, A. Robock, L. Rotstayn, R. Sommerville, G. Stenchikov, Y. Sud, G. Walker, S. Xie, J. Yio, and M. Zhang, A comparison of single column model simulations of summertime midlatitude continental convection. *J. Geophys. Res.*, **105**, 2091-2024, 2000.

Güldner, J. and D. Spänküch, Remote sensing of the thermodynamic state of the atmospheric boundary layer by ground-based microwave radiometry. *J. Atmos. Oceanic Technol.*, **18**, 925-933, 2001.

Liljegren, J. C., E. E. Clothiaux, G. G. Mace, S. Kato, and X. Dong, A new retrieval for cloud liquid water path using a ground-based microwave radiometer and measurements of cloud temperature, *J. Geophys. Res.*, **106**, 14,485-14,500, 2001.

Liljegren, J. C., Automatic self-calibration of ARM microwave radiometers. <u>Microwave Radiometry and Remote Sensing of the Earth's Surface and Atmosphere</u>, edited by P. Pampaloni and S. Paloscia, pp. 433-443, VSP Press, 2000.

Randall, D., S. Krueger, A. Del Genio, S. Ghan, M. Zhang, and R. Cederwall, ARM Vision 2000 as seen by the ARM Cloud Parameterization and Modeling Working Group, DOE ARM Program, 15 pp., 2000.

Rosenkranz, P., Water vapor continuum absorption: a comparison of measurements and models, *Radio Sci*, **33**, 919-928, 1998.

Solheim, F. S., J. R. Godwin, E. R. Westwater, Y. Han, S. J. Keihm, K. March, and R. Ware, Radiometric profiling of temperature, water vapor, and cloud liquid water using various inversion methods. *Radio Sci.*, **33**, 393-404, 1998.

Solheim, F.S., User of pointed water vapor radiometer observations to improve vertical GPS surveying accuracy. Ph.D. Thesis, University of Colorado, 128 pp., 1993.

Smith, W. L., W. F. Feltz, R. O. Knuteson, H. E. Revercomb, H. M. Woolf, and H. B. Howell, The retrieval of planetary boundary layer structure using ground-based infrared spectral radiance measurements. *J. Atmos. Oceanic Technol.,* **16,** 323–333, 1999.